Composite Structures 163 (2017) 152–167

Contents lists available at ScienceDirect

Composite Structures

journal homepage: www.elsevier.com/locate/compstruct

Multi-size unit cells to predict effective thermal conductivities of 3D four-directional braided composites

Jian-Jun Gou [a], Wen-Zhen Fang [a], Yan-Jun Dai [a], Shuguang Li [b], Wen-Quan Tao [a,*]

[a] Key Laboratory of Thermo-Fluid Science and Engineering, Ministry of Education, School of Energy & Power Engineering, Xi'an Jiaotong University, Shaanxi 710049, PR China
[b] Faculty of Engineering, University of Nottingham, Nottingham NG7 2RD, UK

ARTICLE INFO

Article history:
Received 21 June 2016
Revised 24 October 2016
Accepted 5 December 2016
Available online 10 December 2016

Keywords:
Braided composite
Unit cell
Rotational symmetry
Numerical prediction
Effective thermal conductivity

ABSTRACT

Based on the structure of the full unit cell which is formulated by three translational symmetries, three further 180° rotational symmetries of three-dimensional (3D) four-directional braided composites are clarified in this paper. It is for the first time that each rotational symmetry is used to reduce the full unit cell to a half, quarter, and eighth size. The corresponding boundary conditions for thermal analysis are derived precisely according to each rotational transformation. The effective thermal conductivities of composites with different fiber volume fractions and interior braiding angles are calculated by the full, quarter and eighth unit cells. In order to confirm the significance of accurate boundary conditions, additional comparison calculations with adiabatic boundary conditions are conducted and the result reveals that inappropriate boundary conditions may lead to an un-neglectable error in the prediction of thermal conduction behaviours. The numerical model is validated by good agreement between the numerical results and the available experimental ones.

1. Introduction

Three-dimensional (3D) braided composite has been widely studied for its excellent mechanical performance and industry application potential [1–4]. During the production of the composite, the 3D textile should be braided first by a particular braiding process and then solidified with matrix and finally form the composite. The well-known four-step braiding can fabricate 3D four-directional [5], five-directional [6], six-directional and even seven-directional braided textiles [7]. The microstructure of 3D four-directional braided preform and especially the yarns' spatial configuration are analyzed and illustrated according to the braiding process in [5,6]. For the braided composite which is often a periodic structure, its performance is often studied by taking only a representative volume element (unit cell) into account. A unit cell formulated based on the microstructure analysis and the related numerical simulation is a very effective approach used in the study of composites' performance including elastic and shear modulus [8–11], and failure behaviours [12,13]. Similarly, thermal performance of 3D four-directional braided composites can be calculated in the same way [14–17].

As discussed above, the formulation of a unit cell is based on the analysis of the composite microstructure, more specifically it is the geometric symmetries exist in the composite structure that should be identified and analyzed. There are three types of symmetries in the nature, i.e., translations along an axis, reflections about a plane and rotations about an axis. The formulation of a unit cell has two steps: identifying symmetries presented in the composite and deriving corresponding boundary conditions. In relevant works about particle reinforced composites [18], unidirectional fiber reinforced composites [19,20], and several types of woven composites [21–24] symmetries are fully exploited to formulate unit cells of different sizes. However, most studies focus on the mechanical problems and only the corresponding mechanical boundary conditions for unit cells are derived. The thermal problems need thermal boundary conditions. The authors' previous work [25] should be the first time for using unit cells of different sizes to predicting the effective thermal conductivity of plain woven composites, and three reducing-size unit cells are formulated according to translational, reflectional and 180° rotational symmetries and the related thermal boundary conditions are precisely derived. According to the authors' knowledge, for 3D four-directional braided composites most previous works [14–17,26,27] built unit cells by utilizing only the translational symmetries no matter whether it was stated in the papers. A unit cell formulated by translational symmetries can be called a full unit cell.

* Corresponding author.
E-mail address: wqtao@mail.xjtu.edu.cn (W.-Q. Tao).

http://dx.doi.org/10.1016/j.compstruct.2016.12.034
0263-8223/

In the present work, it is for the first time that three 180° rotational symmetries exhibited in the full unit cell are clarified based on the microstructure analysis, and three half, quarter and eighth unit cells are formulated according to the three rotational transformations. Thermal boundary conditions of the unit cells are derived step by step. Numerical models based on the full, quarter and eighth unit cells are established to predict the temperature distributions and the effective thermal conductivities of 3D four-directional braided composites.

2. The formulation of unit cells

Fig. 1(a) shows the schematic diagram of the full unit cell UC_1, and Fig. 1(b) displays the symmetry of several braiding yarns' orientation and will be discussed later. As shown in Fig. 1, the full unit cell UC_1 depicted by black lines is defined by the domain $0 \leqslant x \leqslant a$ & $0 \leqslant y \leqslant b$ & $0 \leqslant z \leqslant h$, the quarter unit cell UC_2 depicted by red lines is defined by the domain $0 \leqslant x \leqslant a/2$ & $0 \leqslant y \leqslant b/2$ & $0 \leqslant z \leqslant h$, while the eighth unit cell UC_3 depicted by blue lines is defined by the domain $0 \leqslant x \leqslant a/4$ & $0 \leqslant y \leqslant b/2$ & $0 \leqslant z \leqslant h$. After a 180° rotation of UC_1 about axis $X_1 = (x, b/2, h/2)$ a half cell shown in Fig. 2 can be formulated, and after a 180° rotation of the half cell about axis $Y_1 = (a/2, y, h/2)$, a quarter unit cell UC_2 shown in Fig. 3 can be formulated. After a 180° rotation of UC_2 about axis $Z_1 = (a/4, b/4, z)$ an eighth unit cell UC_3 can be ultimately formulated and shown in Fig. 4. For the complexity of the geometric structure, it would be necessary to further illustrate three rotational symmetries exhibited in 3D four-directional braided composite.

Before the illustration of the composites' rotational geometric symmetries, the coordinate transformations resulted from a 180° rotation about the axes should be clarified first. It is clear that an arbitrary node $M = (x_1, y_1, z_1)$ will be transformed to node $M' = (x_1, b - y_1, h - z_1)$ by a 180° rotation about axis $X_1 = (x, b/2, h/2)$, to node $M'' = (a - x_1, y_1, h - z_1)$ by a 180° rotation about axis $Y_1 = (a/2, y, h/2)$ and to node $M''' = (a/2 - x_1, b/2 - y_1, z_1)$ by a 180° rotation about axis $Z_1 = (a/4, b/4, z)$. At this condition the rotational geometric symmetries presented in 3D four-directional braided composite can be further illustrated by transformations of two typical braiding yarns L_1 and L_2 (a half segment of the long yarn) in UC_2 as shown in Fig. 1(b). The braiding yarns can be expressed by the coordinates of the start and end points of each yarn, the blue hexagonal and the red circular points in the figures are assumed to be the start point and the end point, respectively. Then we have $L_1 = (0, b/8, h/2) - (a/2, b/8, h)$ and $L_2 = (a/8, 0, 0) - (a/8, b/2, h/2)$. With a 180° rotation about $X_1 = (x, b/2, h/2)$, yarn L_1 will be transformed to $L_1' = (0, 7b/8, h/2) - (a/2, 7b/8, 0)$, with a 180° rotation about $Y_1 = (a/2, y, h/2)$, yarn L_1 will be transformed to $L_1'' = (a, b/8, h/2) - (a/2, b/8, 0)$, and with a 180° rotation about $Z_1 = (a/4, b/4, z)$, yarn L_1 will be transformed to $L_1''' = (a/2, 3b/8, h/2) - (0, 3b/8, h)$. L_2 will be transformed to $L_2' = (a/8, b, h) - (a/8, b/2, h/2)$, $L_2'' = (7a/8, 0, h) - (7a/8, b/2, h/2)$ and $L_2''' = (3a/8, b/2, 0) - (3a/8, 0, h/2)$ by the three 180° rotations, respectively. The coordinate transformations of the two braiding yarns are summarized in Table 1.

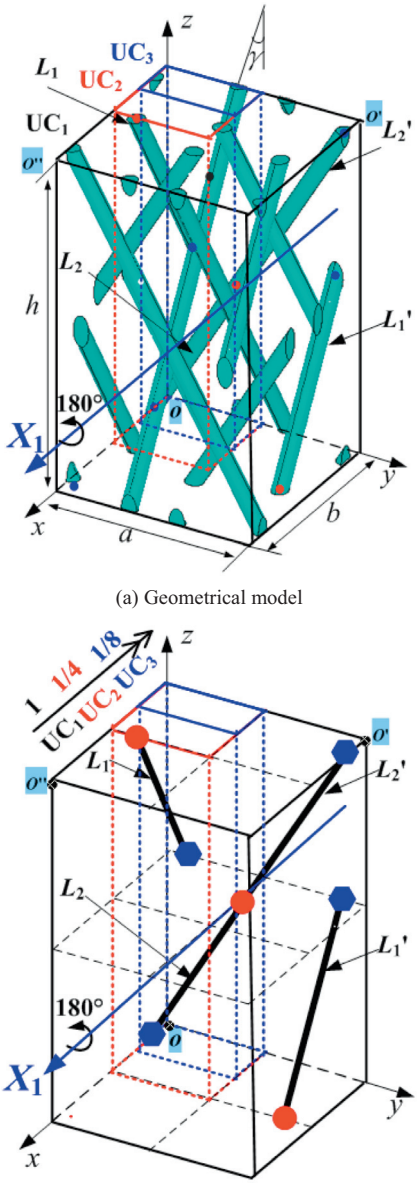

(a) Geometrical model

(b) The symmetry of braiding yarns' orientation

Fig. 1. The full unit cell UC_1.

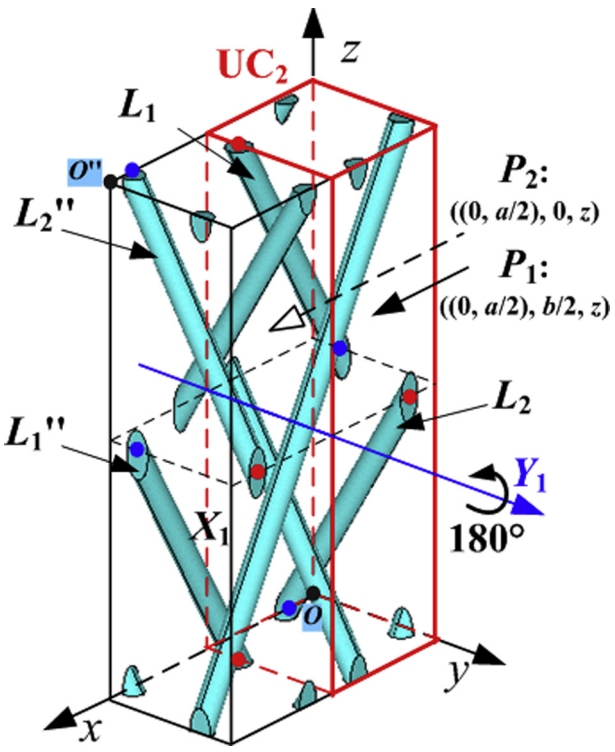

Fig. 2. The half cell.

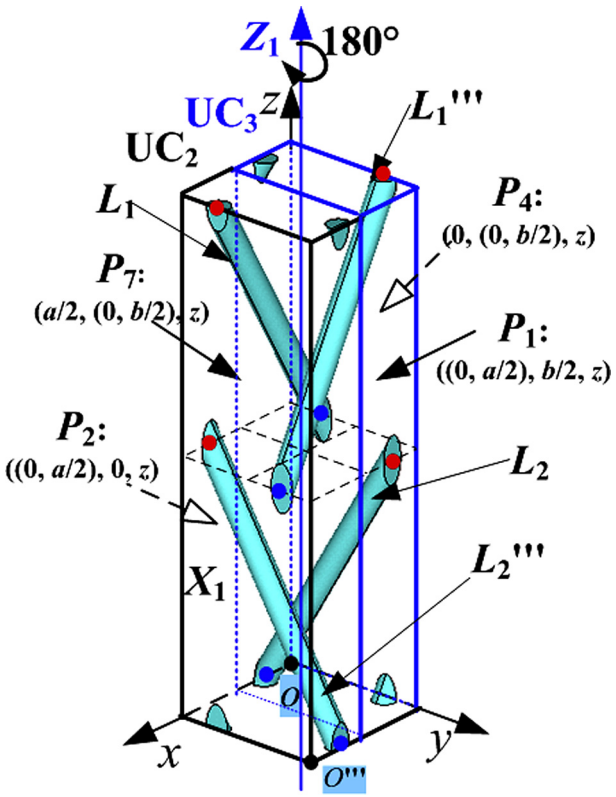

Fig. 3. The quarter unit cell UC_2.

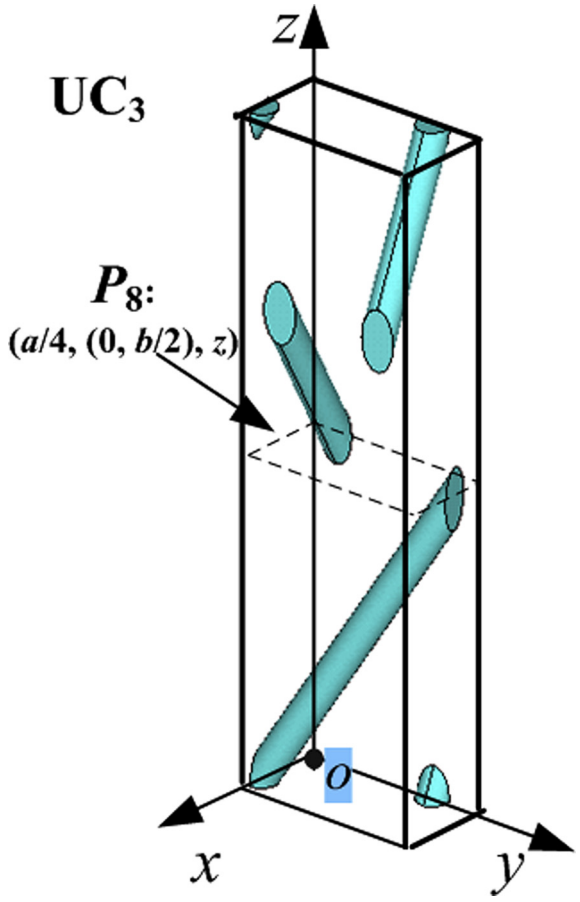

Fig. 4. The eighth unit cell UC_3.

All the corresponding yarns discussed here can be found in UC_1 and are marked in Figs. 1–3. It should be noted that yarns L_2 and L_2' are two half segments of the long yarn (a/8, b, h) – (a/8, 0, 0). In addition, all the other yarns in UC_2 have their corresponding symmetric yarns after the 180° rotational transformations about axes X_1 and Y_1, while every yarn in UC_3 also has its corresponding symmetric yarn after the transformations about axis Z_1, and they will not be stated here for simplicity.

In the later discussion the boundary conditions derivation of the half cell is detailed described, while that of UC_2 and UC_3 have a more concise description. In this work, UC_1, UC_2 and UC_3 are used to conduct numerical simulations and predict the effective thermal conductivities of the composite.

3. Boundary conditions of the full unit cell UC_1

UC_1 is formulated by three translational transformations in x, y and z directions and the so-called periodic boundary conditions can be adopted in three cases, i.e., the calculation of effective thermal conductivity in three directions λ_{xx}, λ_{yy} and λ_{zz} as follows:

For the calculation of λ_{xx}, the temperature gradient in x direction, $T_x^o = \Delta T/a$ is adopted, and the boundary conditions can be described as:

$$\begin{aligned} T_{(0,y_1,z_1)} - T_{(a,y_1,z_1)} &= \Delta T, T_{(x_1,0,z_1)} - T_{(x_1,b,z_1)} \\ &= 0, T_{(x_1,y_1,0)} - T_{(x_1,y_1,h)} = 0 \end{aligned} \tag{1}$$

For the calculation of λ_{yy}, we have boundary conditions:

$$\begin{aligned} T_{(0,y_1,z_1)} - T_{(a,y_1,z_1)} &= 0, T_{(x_1,0,z_1)} - T_{(x_1,b,z_1)} \\ &= \Delta T, T_{(x_1,y_1,0)} - T_{(x_1,y_1,h)} = 0 \end{aligned} \tag{2}$$

For the calculation of λ_{zz}, we have boundary conditions:

$$\begin{aligned} T_{(0,y_1,z_1)} - T_{(a,y_1,z_1)} &= 0, T_{(x_1,0,z_1)} - T_{(x_1,b,z_1)} \\ &= 0, T_{(x_1,y_1,0)} - T_{(x_1,y_1,h)} = \Delta T \end{aligned} \tag{3}$$

where a, b and h in the subscripts are the length, width and height of the unit cell as shown in Fig. 1. In addition, boundary conditions of nodes on vertices and edges which can be derived from Eqs. (1) to (3) are detailed described in Reference [16]. ΔT in this paper is assumed to be 20 °C.

It should be noted that boundary conditions of UC_2 and UC_3 discussed later are derived based on that of UC_1.

4. Relative temperature relations resulted from 180° rotational transformations

Before the derivation of boundary conditions of UC_2 and UC_3, the symmetric and antisymmetric thermal stimuli should be stated first. As introduced in the authors' previous work [25], the heat flux parallel to the rotation axis can be considered as symmetric thermal stimulus (STS), while the one perpendicular to the rotation axis can be considered as antisymmetric stimulus (ATS). Take the half cell which is formulated by a rotational transformation about axis X_1 as an example, for the calculation of λ_{xx} the heat flux is parallel to axis X_1 and thus can be considered as a symmetric thermal stimulus, while for the calculation of λ_{yy} and λ_{zz} the heat flux is perpendicular to axis X_1 and thus can be considered as an antisymmetric thermal stimulus. Under these two conditions, the relative temperature relations between the corresponding symmetric nodes M and M' can be described as:

$$\text{STS}: T_M - T_O = T_{M'} - T_{O'} \tag{4}$$

$$\text{ATS}: T_M - T_O = T_{O'} - T_{M'} \tag{5}$$

Table 1
The coordinate transformations of the braiding yarns L_1 and L_2.

180° rotational axes	$X_1 = (x, b/2, h/2)$	$Y_1 = (a/2, y, h/2)$	$Z_1 = (a/4, b/4, z)$
$M = (x_1, y_1, z_1)$	$M' = (x_1, b - y_1, h - z_1)$	$M'' = (a - x_1, y_1, h - z_1)$	$M''' = (a/2 - x_1, b/2 - y_1, z_1)$
$L_1 = (0, b/8, h/2) - (a/2, b/8, h)$	$L_1' = (0, 7b/8, h/2) - (a/2, 7b/8, 0)$	$L_1'' = (a, b/8, h/2) - (a/2, b/8, 0)$	$L_1''' = (a/2, 3b/8, h/2) - (0, 3b/8, h)$
$L_2 = (a/8, 0, 0) - (a/8, b/2, h/2)$	$L_2' = (a/8, b, h) - (a/8, b/2, h/2)$	$L_2'' = (7a/8, 0, h) - (7a/8, b/2, h/2)$	$L_2''' = (3a/8, b/2, 0) - (3a/8, 0, h/2)$

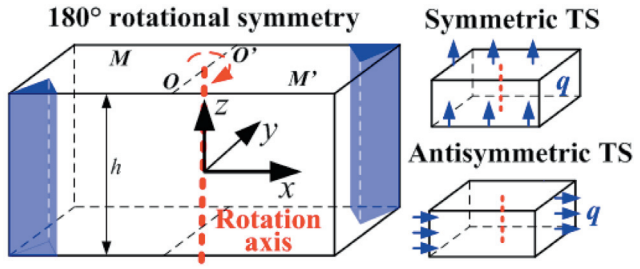

(a) Rotational symmetry and two types of thermal stimuli

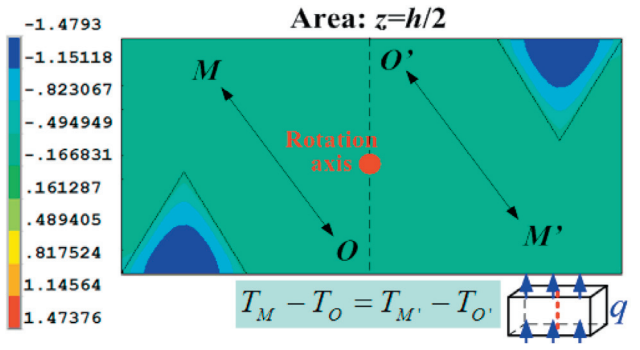

(b) Temperature fields under symmetric thermal stimulus

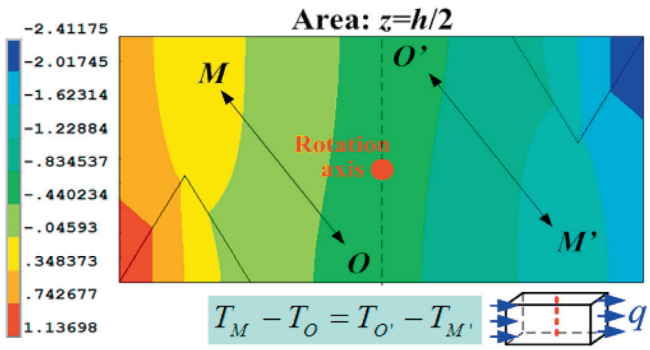

(c) Temperature fields under antisymmetric thermal stimulus

Fig. 5. Relative temperature relations resulted from 180° rotational transformation.

where T_M, T_O, $T_{M'}$ and $T_{O'}$ are the temperatures of each node, respectively. T_O and $T_{O'}$ can be considered as reference temperatures. It is clear that when the arbitrary node M is locating on a boundary plane, Eqs. (4) or (5) can be used to derive boundary conditions of this plane.

Fig. 5 shows the confirmation of Eqs. (4) and (5) by a simple calculation case. Fig. 5(a) shows the structure which has a 180° rotational symmetry and the two types of thermal stimuli, and Figs. 5(b) and (c) show the temperature fields that resulted from different thermal stimuli. In Fig. 5(a) the thick red dash line is the rotational axis and "TS" means thermal stimulus. The arbitrary node M and the reference node O and their corresponding symmetric nodes after rotational transformation M' and O' can be found in the figure. The blue prism region (see Fig. 5(a)) has a thermal conductivity of 1 W/(m·K), while the rest region has a value of 10 W/(m·K). Two cases of calculations have been conducted, i.e., the heat flux in x- and z-direction which can be considered as symmetric and antisymmetric thermal stimuli, respectively, and the obtained temperature fields are displayed in Fig. 5(b) and (c), respectively. In the calculations, $q = 10\ \mathrm{W/m^2}$ on the boundary planes in the calculation direction and boundary conditions of other planes are adiabatic. The calculated temperature fields of planes $z = h/2$ are displayed in Figs. 5(b) and (c). It is clear that the relative temperature relations described by Eqs. (4) and (5) are satisfied by temperature distributions shown in Figs. 5(b) and (c), respectively.

All the later derivation of boundary conditions is based on Eqs. (4) and (5). However, as summarized in Table 2, different unit cells and simulation cases corresponding to different equations because of their specific conditions of thermal stimulus. The boundary conditions of each unit cell are derived separately in following sections. Although the following derivation process seems to be complicated and tedious, if one can do the derivation himself along with the process described in this paper, the derivation would be easy to understand for sure.

5. Boundary conditions of the half unit cell

In order to have a clear description, the boundaries of unit cells are denoted by numbers as shown in Fig. 6. In the figure, the hollow circles with numbers represent vertices, the black circles with numbers represent edges, while P_1 to P_8 represent the boundary planes. P_3, P_7 and P_8 denote boundary planes in the same direction of half cell, UC_2 and UC_3, respectively.

Table 2
The relative temperature relations between symmetric nodes in different cases.

Rot. axes	Nodes coordinates	Cal. cases	Thermal stimulus	Relative temperature relations	BC of UC_1
$X_1 = (x, b/2, h/2)$ (half cell)	$M = (x_1, y_1, z_1) \rightarrow M' = (x_1, b - y_1, h - z_1)$	λ_{xx}	STS	Eq. (4)	Eq. (1)
		λ_{yy}	ATS	Eq. (5)	Eq. (2)
		λ_{zz}	ATS	Eq. (5)	Eq. (3)
$Y_1 = (a/2, y, h/2)$ (UC_2)	$M = (x_1, y_1, z_1) \rightarrow M'' = (a - x_1, y_1, h - z_1)$	λ_{xx}	ATS	Eq. (5)	Eq. (1)
		λ_{yy}	STS	Eq. (4)	Eq. (2)
		λ_{zz}	ATS	Eq. (5)	Eq. (3)
$Z_1 = (a/4, b/4, z)$ (UC_3)	$M = (x_1, y_1, z_1) \rightarrow M''' = (a/2 - x_1, b/2 - y_1, z_1)$	λ_{xx}	ATS	Eq. (5)	Eq. (1)
		λ_{yy}	ATS	Eq. (5)	Eq. (2)
		λ_{zz}	STS	Eq. (4)	Eq. (3)

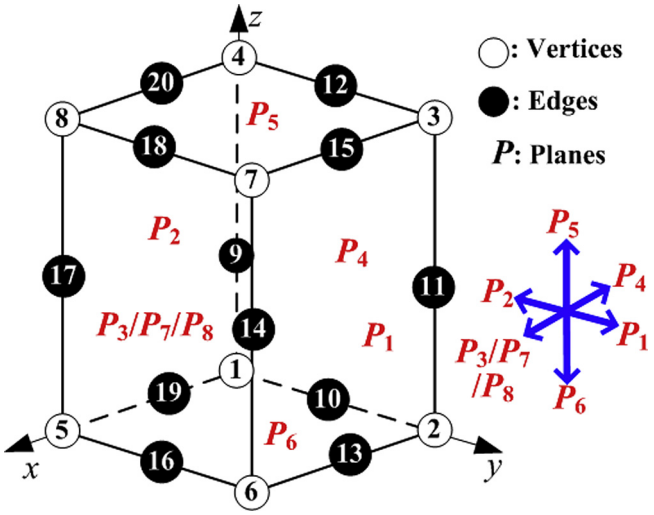

Fig. 6. Boundaries of the half cell, UC_2 and UC_3.

As can be seen in Figs. 1 and 2, the half cell is formulated by a 180° rotation about X_1 axis which generates boundary planes $P_1 = ((0, a/2), b/2, z)$ and $P_2 = ((0, a/2), 0, z)$ (see Fig. 2). Boundary conditions of boundary planes P_3 ($x = a$), P_4 ($x = 0$), P_5 ($z = h$) and P_6 ($z = 0$) are the same with that of UC_1. As discussed above the assumed arbitrary node $M = (x_1, y_1, z_1)$ in the half cell can be transformed to node $M' = (x_1, b - y_1, h\text{-}z_1)$. Taking node $O = (0, 0, 0)$ as an example, it will be transformed to $O' = (0, b, h)$ as shown in Fig. 1 and Fig. 2. In this work the boundary conditions are derived in three cases, i.e. the calculation of effective thermal conductivity in x direction λ_{xx}, in y direction λ_{yy} and in z direction λ_{zz}.

5.1. The calculation of λ_{xx}

As shown in Table 2, in this case the boundary conditions for planes P_3 to P_6 are presented in Eq. (1). Therefore, only boundary planes $P_1 = ((0, a/2), b/2, z)$ and $P_2 = ((0, a/2), 0, z)$ need to be considered. As shown in Table 2 the heat flux can be considered as a symmetric thermal stimulus. The relative temperature relations between the assumed arbitrary node $M = (x_1, y_1, z_1)$ and the transformed node $M' = (x_1, b - y_1, h - z_1)$ can be described by Eq. (4).

5.1.1. Boundary conditions of plane P_1

When it comes to the boundary plane $P_1 = ((0, a/2), b/2, z)$, we can have nodes $M = (x_1, b/2, z_1)$ and $M' = (x_1, b/2, h - z_1)$. T_M and $T_{M'}$ can be respectively represented by $T_{(x_1,b/2,z_1)}$ and $T_{(x_1,b/2,h-z_1)}$. With additional temperature relations between the reference nodes $T_{O=(0,0,0)} = T_{(0,b,0)} = T_{O'=(0,b,h)}$ (obtained from Eq. (1)), Eq. (4) becomes the boundary conditions of boundary plane P_1:

$$T_{(x_1,b/2,z_1)} = T_{(x_1,b/2,h-z_1)} \tag{6}$$

5.1.2. Boundary conditions of plane P_2

On the other hand, when the node comes to the boundary plane $P_2 = ((0, a/2), 0, z)$, we can have $M = (x_1, 0, z_1)$ and $M' = (x_1, b, h - z_1)$. T_M and $T_{M'}$ can be represented by $T_{(x_1,0,z_1)}$ and $T_{(x_1,b,h-z_1)}$, respectively. With additional $T_{O=(0,0,0)} = T_{(0,b,0)} = T_{O'=(0,b,h)}$, Eq. (4) becomes:

$$T_{(x_1,0,z_1)} = T_{(x_1,b,h-z_1)} \tag{7}$$

It is obvious that $T_{(x_1,b,h-z_1)}$ represents temperature of a node not located in the half cell so the boundary condition needs more derivation. Considering the periodic boundary conditions described in Eq. (1), we can easily have:

$$T_{(x_1,0,h-z_1)} = T_{(x_1,b,h-z_1)} \tag{8}$$

Based on Eqs. (7) and (8), boundary conditions of plane P_2 can be described as:

$$T_{(x_1,0,z_1)} = T_{(x_1,0,h-z_1)} \tag{9}$$

5.1.3. Boundary conditions of the half cell

Based on Eqs. (1), (6) and (9), boundary conditions of the half cell for the calculation of effective thermal conductivities in x direction can be summarized as:

$$\begin{aligned}
&\boldsymbol{P_1}: T_{(x_1,b/2,z_1)} = T_{(x_1,b/2,h-z_1)},\\
&\boldsymbol{P_2}: T_{(x_1,0,z_1)} = T_{(x_1,0,h-z_1)},\\
&\boldsymbol{P_4} - \boldsymbol{P_3}: T_{(0,y_1,z_1)} - T_{(a,y_1,z_1)} = \Delta T,\\
&\boldsymbol{P_6} - \boldsymbol{P_5}: T_{(x_1,y_1,0)} - T_{(x_1,y_1,h)} = 0
\end{aligned} \tag{10}$$

5.2. The calculation of λ_{yy}

In this case, as listed in Table 2 boundary conditions for planes P_3 to P_6 are presented in Eq. (2). The heat flux can be considered as an antisymmetric thermal stimulus and the relative temperature relation between $M = (x_1, y_1, z_1)$ and $M' = (x_1, b - y_1, h - z_1)$ is described by Eq. (5).

5.2.1. Boundary conditions of plane P_1

When it comes to the boundary plane P_1 (plane: $y = b/2$), T_M and $T_{M'}$ can be respectively represented by $T_{(x_1,b/2,z_1)}$ and $T_{(x_1,b/2,h-z_1)}$, with the additional temperature relation between the reference nodes $T_{O=(0,0,0)} = T_{(0,b,0)} + \Delta T = T_{O'=(0,b,h)} + \Delta T$ (obtained from Eq. (2)), Eq. (5) becomes the boundary conditions of boundary plane P_1:

$$T_{(x_1,b/2,z_1)} + T_{(x_1,b/2,h-z_1)} = 2T_{(0,0,0)} - \Delta T \tag{11}$$

where $T_{(0,0,0)}$ represents the temperature of reference node $O = (0, 0, 0)$.

5.2.2. Boundary conditions of plane P_2

When node M comes to the boundary plane P_2 (plane: $y = 0$), T_M and $T_{M'}$ can be respectively represented by $T_{(x_1,0,z_1)}$ and $T_{(x_1,b,h-z_1)}$, Eq. (5) becomes:

$$T_{(x_1,0,z_1)} + T_{(x_1,b,h-z_1)} = 2T_{(0,0,0)} - \Delta T \tag{12}$$

As discussed above, $T_{(x_1,b,h-z_1)}$ represents temperature of a node not located in the half cell so the boundary condition needs more derivation. Considering the periodic boundary conditions described in Eq. (2), we can have:

$$T_{(x_1,0,h-z_1)} = T_{(x_1,b,h-z_1)} + \Delta T \tag{13}$$

Based on Eqs. (12) and (13), boundary conditions for plane P_2 can be described as:

$$T_{(x_1,0,z_1)} + T_{(x_1,0,h-z_1)} = 2T_{(0,0,0)} \tag{14}$$

5.2.3. Boundary conditions of the half cell

Based on Eqs. (2), (11) and (14), the boundary conditions of the half cell for the calculation of effective thermal conductivities in y direction can be summarized as:

$$\begin{aligned}
&\boldsymbol{P_1}: T_{(x_1,b/2,z_1)} + T_{(x_1,b/2,h-z_1)} = 2T_{(0,0,0)} - \Delta T,\\
&\boldsymbol{P_2}: T_{(x_1,0,z_1)} + T_{(x_1,0,h-z_1)} = 2T_{(0,0,0)},\\
&\boldsymbol{P_4} - \boldsymbol{P_3}: T_{(0,y_1,z_1)} - T_{(a,y_1,z_1)} = 0,\\
&\boldsymbol{P_6} - \boldsymbol{P_5}: T_{(x_1,y_1,0)} - T_{(x_1,y_1,h)} = 0
\end{aligned} \tag{15}$$

In this equation, node $O = (0, 0, 0)$ can be considered as a reference node.

5.3. The calculation of λ_{zz}

In this case, as listed in Table 2 boundary conditions for plane P_3 to P_6 are presented in Eq. (3). The heat flux can be considered as an antisymmetric thermal stimulus and the relative temperature relation between $M = (x_1, y_1, z_1)$ and $M' = (x_1, b - y_1, h - z_1)$ is described by Eq. (5).

5.3.1. Boundary conditions of plane P_1

When node M comes to the boundary plane (plane: $y = b/2$), with additional $T_{O=(0,0,0)} = T_{(0,b,0)} = T_{O'=(0,b,h)} + \Delta T$ (obtained from Eq. (3)) we can have boundary conditions defined by Eq. (11).

5.3.2. Boundary conditions of plane P_2

When node M comes to the boundary plane P_2 (plane: $y = 0$), T_M and $T_{M'}$ can be respectively represented by $T_{(x_1,0,z_1)}$ and $T_{(x_1,b,h-z_1)}$, then Eq. (5) has a form of Eq. (12), and considering the periodic boundary conditions described in Eq. (3), we can have:

$$T_{(x_1,0,z_1)} = T_{(x_1,b,h-z_1)} \tag{16}$$

It should be noted that Eq. (16) has the same form with Eq. (8) although they are derived from different equations. Based on Eqs. (12) and (16), boundary conditions for plane P_2 can be described as:

$$T_{(x_1,0,z_1)} + T_{(x_1,0,h-z_1)} = 2T_{(0,0,0)} - \Delta T \tag{17}$$

5.3.3. Boundary conditions of the half cell

Based on Eqs. (3), (11) and (17) the boundary conditions of the half cell for the calculation of effective thermal conductivities in z direction can thus be summarized as:

$$\begin{aligned}
&\boldsymbol{P_1}: T_{(x_1,b/2,z_1)} + T_{(x_1,b/2,h-z_1)} = 2T_{(0,0,0)} - \Delta T,\\
&\boldsymbol{P_2}: T_{(x_1,0,z_1)} + T_{(x_1,0,h-z_1)} = 2T_{(0,0,0)} - \Delta T,\\
&\boldsymbol{P_4} - \boldsymbol{P_3}: T_{(0,y_1,z_1)} - T_{(a,y_1,z_1)} = 0,\\
&\boldsymbol{P_6} - \boldsymbol{P_5}: T_{(x_1,y_1,0)} - T_{(x_1,y_1,h)} = \Delta T
\end{aligned} \tag{18}$$

6. Boundary conditions of the quarter unit cell UC_2

The quarter unit cell UC_2 (see Fig. 3) will be formulated by a further rotational transformation, i.e., a 180° rotation about Y_1 axis and generates a new boundary plane $P_7 = (a/2, (0, b/2), z)$. In this case, the boundary conditions for planes P_1 ($y = b/2$), P_2 ($y = 0$), P_5 ($z = h$) and P_6 ($z = 0$) are presented in Eqs. (10), (15) and (18), respectively. Therefore, only boundary planes $P_7 = (a/2, (0, b/2), z)$ and $P_4 = (0, (0, b/2, z))$ need to be considered. The reference node $O = (0, 0, 0)$ will be transformed to $O'' = (a, 0, h)$ as shown in Figs. 1 and 2. The derivation of boundary conditions is in much a similar way with that of the half cell. And a concise derivation process is summarized in Table 3.

In ANSYS, nodes on vertices and edges of unit cells should be considered separately to avoid the redundant constraints that may influence the proper operation. Therefore, based on equations in Table 3 boundary conditions of UC_2 for calculations of λ_{xx}, λ_{yy} and λ_{zz} can be finally summarized as Eqs. (19)–(21), respectively. The vertices and edges of unit cell are shown in Fig. 6, and the edges are classified into three groups in these equations according to their directions.

For the calculation of λ_{xx}:

Table 3
The derivation process of boundary conditions of UC_2.

Cal. cases	Boundary planes	Boundary conditions
λ_{xx}	P_1, P_2, P_5, P_6	Eq. (10) $\rightarrow$ $\boldsymbol{P_1}: T_{(x_1,b/2,z_1)} - T_{(x_1,b/2,h-z_1)} = 0$ $\boldsymbol{P_2}: T_{(x_1,0,z_1)} - T_{(x_1,0,h-z_1)} = 0$ $\boldsymbol{P_6} - \boldsymbol{P_5}: T_{(x_1,y_1,0)} - T_{(x_1,y_1,h)} = 0$
	$P_4 = (0, (0, b/2, z))$	$\begin{cases}\text{Eq. (5)} \rightarrow T_M - T_O = T_{O''} - T_{M''} \rightarrow \\ T_{(0,y_1,z_1)} - T_{O=(0,0,0)} = T_{O''=(a,0,h)} - T_{(a,y_1,h-z_1)} \\ \text{Eq. (1)} \Rightarrow T_O = T_{(a,0,0)} + \Delta T = T_{O''} + \Delta T \\ \text{Eq. (1)} \Rightarrow T_{(0,y_1,h-z_1)} = T_{(a,y_1,h-z_1)} + \Delta T \end{cases}$ $\Rightarrow T_{(0,y_1,z_1)} + T_{(0,y_1,h-z_1)} = 2T_{O=(0,0,0)}$
	$P_7 = (a/2, (0, b/2), z)$	$\begin{cases}\text{Eq. (5)} \rightarrow T_{(a/2,y_1,z_1)} - T_{O=(0,0,0)} = T_{O''=(a,0,h)} - T_{(a/2,y_1,h-z_1)} \\ \text{Eq. (1)} \Rightarrow T_O = T_{(a,0,0)} + \Delta T = T_{O''} + \Delta T \end{cases}$ $\Rightarrow T_{(a/2,y_1,z_1)} + T_{(a/2,y_1,h-z_1)} = 2T_{O=(0,0,0)} - \Delta T$
λ_{yy}	P_1, P_2, P_5, P_6	Eq. (15) $\rightarrow$ $\boldsymbol{P_1}: T_{(x_1,b/2,z_1)} + T_{(x_1,b/2,h-z_1)} - 2T_{(0,0,0)} = -\Delta T$ $\boldsymbol{P_2}: T_{(x_1,0,z_1)} + T_{(x_1,0,h-z_1)} - 2T_{(0,0,0)} = 0$ $\boldsymbol{P_6} - \boldsymbol{P_5}: T_{(x_1,y_1,0)} - T_{(x_1,y_1,h)} = 0$
	$P_4 = (0, (0, b/2, z))$	$\begin{cases}\text{Eq. (4)} \rightarrow T_M - T_O = T_{M''} - T_{O''} \rightarrow \\ T_{(0,y_1,z_1)} - T_{O=(0,0,0)} = T_{(a,y_1,h-z_1)} - T_{O''=(a,0,h)} \\ \text{Eq. (2)} \Rightarrow T_O = T_{(a,0,0)} = T_{O''} \\ \text{Eq. (2)} \Rightarrow T_{(a,y_1,h-z_1)} = T_{(0,y_1,h-z_1)} \end{cases}$ $\Rightarrow T_{(0,y_1,z_1)} = T_{(0,y_1,h-z_1)}$
	$P_7 = (a/2, (0, b/2), z)$	$\begin{cases}\text{Eq. (4)} \rightarrow T_{(a/2,y_1,z_1)} - T_{O=(0,0,0)} = T_{(a/2,y_1,h-z_1)} - T_{O''=(a,0,h)} \\ \text{Eq. (2)} \Rightarrow T_O = T_{(a,0,0)} = T_{O''} \end{cases}$ $\Rightarrow T_{(a/2,y_1,z_1)} = T_{(a/2,y_1,h-z_1)}$
λ_{zz}	P_1, P_2, P_5, P_6	Eq. (18) $\rightarrow$ $\boldsymbol{P_1}: T_{(x_1,b/2,z_1)} + T_{(x_1,b/2,h-z_1)} - 2T_{(0,0,0)} = -\Delta T$ $\boldsymbol{P_2}: T_{(x_1,0,z_1)} + T_{(x_1,0,h-z_1)} - 2T_{(0,0,0)} = -\Delta T$ $\boldsymbol{P_6} - \boldsymbol{P_5}: T_{(x_1,y_1,0)} - T_{(x_1,y_1,h)} = \Delta T$
	$P_4 = (0, (0, b/2, z))$	$\begin{cases}\text{Eq. (5)} \rightarrow T_{(0,y_1,z_1)} - T_{O=(0,0,0)} = T_{O''=(a,0,h)} - T_{(a,y_1,h-z_1)} \\ \text{Eq. (3)} \Rightarrow T_O = T_{(a,0,0)} = T_{O''} + \Delta T \\ \text{Eq. (3)} \Rightarrow T_{(a,y_1,h-z_1)} = T_{(0,y_1,h-z_1)} \end{cases}$ $\Rightarrow T_{(0,y_1,z_1)} + T_{(0,y_1,h-z_1)} = 2T_{(0,0,0)} - \Delta T$
	$P_7 = (a/2, (0, b/2), z)$	$\begin{cases}\text{Eq. (5)} \rightarrow T_{(a/2,y_1,z_1)} - T_{O=(0,0,0)} = T_{O''=(a,0,h)} - T_{(a/2,y_1,h-z_1)} \\ \text{Eq. (3)} \Rightarrow T_O = T_{(a,0,0)} = T_{O''} + \Delta T \end{cases}$ $\Rightarrow T_{(a/2,y_1,z_1)} + T_{(a/2,y_1,h-z_1)} = 2T_{O=(0,0,0)} - \Delta T$

Boundary planes :

$$\boldsymbol{P_1}: T_{(x_1,b/2,z_1)} - T_{(x_1,b/2,h-z_1)} = 0$$
$$\boldsymbol{P_2}: T_{(x_1,0,z_1)} - T_{(x_1,0,h-z_1)} = 0$$
$$\boldsymbol{P_4}: T_{(0,y_1,z_1)} + T_{(0,y_1,h-z_1)} - 2T_{O=(0,0,0)} = 0$$
$$\boldsymbol{P_7}: T_{(a/2,y_1,z_1)} + T_{(a/2,y_1,h-z_1)} - 2T_{O=(0,0,0)} = -\Delta T$$
$$\boldsymbol{P_6} - \boldsymbol{P_5}: T_{(x_1,y_1,0)} - T_{(x_1,y_1,h)} = 0$$

Vertices :

$$T_{1=(0,0,0)} = T_{(0,0,0)}, T_{2=(0,b/2,0)} - T_{(0,0,0)} = 0,$$
$$T_{3=(0,b/2,h)} - T_{(0,0,0)} = 0, T_{4=(0,0,h)} - T_{(0,0,0)} = 0,$$
$$T_{5=(a/2,0,0)} - T_{(0,0,0)} = -\Delta T/2, T_{6=(a/2,b/2,0)} - T_{(0,0,0)} = -\Delta T/2,$$
$$T_{7=(a/2,b/2,h)} - T_{(0,0,0)} = -\Delta T/2, T_{8=(a/2,0,h)} - T_{(0,0,0)} = -\Delta T/2$$

Edges parallel to $\boldsymbol{z}$ axis :

$$T_{9=(0,0,z_1)} - T_{(0,0,0)} = 0, T_{11=(0,b/2,z_1)} - T_{(0,0,0)} = 0,$$
$$T_{14=(a/2,b/2,z_1)} - T_{(0,0,0)} = -\Delta T/2, T_{17=(a/2,0,z_1)} - T_{(0,0,0)} = -\Delta T/2$$

Edges parallel to $\boldsymbol{y}$ axis :

$$T_{10=(0,y_1,0)} - T_{(0,0,0)} = 0, T_{12=(0,y_1,h)} - T_{(0,0,0)} = 0,$$
$$T_{16=(a/2,y_1,0)} - T_{(0,0,0)} = -\Delta T/2, T_{18=(a/2,y_1,h)} - T_{(0,0,0)} = -\Delta T/2$$

Edges parallel to x axis :

$$T_{13=(x_1,b/2,0)} - T_{15=(x_1,b/2,h)} = 0, T_{19=(x_1,0,0)} - T_{20=(x_1,0,h)} = 0 \quad (19)$$

For the calculation of λ_{yy}:

Boundary planes :

$$\boldsymbol{P_1}: T_{(x_1,b/2,z_1)} + T_{(x_1,b/2,h-z_1)} - 2T_{(0,0,0)} = -\Delta T$$
$$\boldsymbol{P_2}: T_{(x_1,0,z_1)} + T_{(x_1,0,h-z_1)} - 2T_{(0,0,0)} = 0$$
$$\boldsymbol{P_4}: T_{(0,y_1,z_1)} - T_{(0,y_1,h-z_1)} = 0$$
$$\boldsymbol{P_7}: T_{(a/2,y_1,z_1)} - T_{(a/2,y_1,h-z_1)} = 0$$
$$\boldsymbol{P_6} - \boldsymbol{P_5}: T_{(x_1,y_1,0)} - T_{(x_1,y_1,h)} = 0$$

Vertices :

$$T_{1=(0,0,0)} = T_{(0,0,0)}, \ T_{2=(0,b/2,0)} - T_{(0,0,0)} = -\Delta T/2,$$
$$T_{3=(0,b/2,h)} - T_{(0,0,0)} = -\Delta T/2,$$
$$T_{4=(0,0,h)} - T_{(0,0,0)} = 0, \ T_{5=(a/2,0,0)} - T_{(0,0,0)} = 0,$$
$$T_{6=(a/2,b/2,0)} - T_{(0,0,0)} = -\Delta T/2,$$
$$T_{7=(a/2,b/2,h)} - T_{(0,0,0)} = -\Delta T/2, \ T_{8=(a/2,0,h)} - T_{(0,0,0)} = 0$$

Edges parallel to z axis :

$$T_{9=(0,0,z_1)} - T_{(0,0,0)} = 0, \ T_{11=(0,b/2,z_1)} - T_{(0,0,0)} = -\Delta T/2,$$
$$T_{14=(a/2,b/2,z_1)} - T_{(0,0,0)} = -\Delta T/2, \ T_{17=(a/2,0,z_1)} - T_{(0,0,0)} = 0$$

Edges parallelto y axis :

$$T_{10=(0,y_1,0)} - T_{12=(0,y_1,h)} = 0, \ T_{16=(a/2,y_1,0)} - T_{18=(a/2,y_1,h)} = 0$$

Edges parallel to x axis :

$$T_{13=(x_1,b/2,0)} - T_{(0,0,0)} = -\Delta T/2, \ T_{15=(x_1,b/2,h)} - T_{(0,0,0)} = -\Delta T/2,$$
$$T_{19=(x_1,0,0)} - T_{(0,0,0)} = 0, \ T_{20=(x_1,0,h)} - T_{(0,0,0)} = 0 \quad (20)$$

For the calculation of λ_{zz}:

Boundary planes :

$$\boldsymbol{P_1}: T_{(x_1,b/2,z_1)} + T_{(x_1,b/2,h-z_1)} - 2T_{(0,0,0)} = -\Delta T$$
$$\boldsymbol{P_2}: T_{(x_1,0,z_1)} + T_{(x_1,0,h-z_1)} - 2T_{(0,0,0)} = -\Delta T$$
$$\boldsymbol{P_4}: T_{(0,y_1,z_1)} + T_{(0,y_1,h-z_1)} - 2T_{(0,0,0)} = -\Delta T$$
$$\boldsymbol{P_7}: T_{(a/2,y_1,z_1)} + T_{(a/2,y_1,h-z_1)} - 2T_{(0,0,0)} = -\Delta T$$
$$\boldsymbol{P_6} - \boldsymbol{P_5}: T_{(x_1,y_1,0)} - T_{(x_1,y_1,h)} = \Delta T$$

Vertices :

$$T_{1=(0,0,0)} = T_{(0,0,0)}, \ T_{2=(0,b/2,0)} - T_{(0,0,0)} = 0,$$
$$T_{3=(0,b/2,h)} - T_{(0,0,0)} = -\Delta T/2,$$
$$T_{4=(0,0,h)} - T_{(0,0,0)} = -\Delta T/2, \ T_{5=(a/2,0,0)} - T_{(0,0,0)} = 0,$$
$$T_{6=(a/2,b/2,0)} - T_{(0,0,0)} = 0,$$
$$T_{7=(a/2,b/2,h)} - T_{(0,0,0)} = -\Delta T/2, \ T_{8=(a/2,0,h)} - T_{(0,0,0)} = -\Delta T/2$$

Edges parallel to z axis :

$$T_{9=(0,0,z_1)} + T_{9=(0,0,h-z_1)} - 2T_{(0,0,0)} = -\Delta T,$$
$$T_{11=(0,b/2,z_1)} + T_{11=(0,b/2,h-z_1)} - 2T_{(0,0,0)} = -\Delta T,$$
$$T_{14=(a/2,b/2,z_1)} + T_{14=(a/2,b/2,h-z_1)} - 2T_{(0,0,0)} = -\Delta T,$$
$$T_{17=(a/2,0,z_1)} + T_{17=(a/2,0,h-z_1)} - 2T_{(0,0,0)} = -\Delta T,$$

Edges parallel to y axis :

$$T_{10=(0,y_1,0)} - T_{(0,0,0)} = 0, \ T_{12=(0,y_1,h)} - T_{(0,0,0)} = -\Delta T,$$
$$T_{16=(a/2,y_1,0)} - T_{(0,0,0)} = 0, \ T_{18=(a/2,y_1,h)} - T_{(0,0,0)} = -\Delta T$$

Edges parallel to x axis :

$$T_{13=(x_1,b/2,0)} - T_{(0,0,0)} = 0, \ T_{15=(x_1,b/2,h)} - T_{(0,0,0)} = -\Delta T,$$
$$T_{19=(x_1,0,0)} - T_{(0,0,0)} = 0, \ T_{20=(x_1,0,h)} - T_{(0,0,0)} = -\Delta T \quad (21)$$

7. Boundary conditions of the eighth unit cell UC_3

An eighth unit cell UC_3 (see Fig. 4) will be formulated by a further 180° rotational transformation of UC_2 about Z_1 axis (see Fig. 3), and this process also generates a new boundary plane $P_8 = (a/4, (0, b/2), z)$. In this case, the boundary conditions for planes P_1 ($y = b/2$), P_2 ($y = 0$), P_4 ($x = 0$), P_5 ($z = h$) and P_6 ($z = 0$) are presented in Eqs. (19)–(21), respectively. Therefore, only boundary conditions of plane $P_8 = (a/4, (0, b/2), z)$ need to be derived. The reference node $O = (0, 0, 0)$ will be transformed to $O'' = (a/2, b/2, 0)$ as shown in Fig. 3. Based on Eqs. (1) to (5) (see Table 2) and Eqs. (19) to (21) the derivation process can be concisely summarized in Table 4.

Based on equations in Table 4, considering the separate constraint equations of nodes on vertices and edges, boundary conditions of UC_3 for calculations of λ_{xx}, λ_{yy} and λ_{zz} can be finally summarized as Eqs. (22)–(24), respectively. Although boundary conditions of planes P_1, P_2, P_4, P_5 and P_6 of UC_3 have the same forms with UC_2, they are still displayed in Eqs. (22)–(24).

For the calculation of λ_{xx}:

Boundary planes :

$$\boldsymbol{P_1}: T_{(x_1,b/2,z_1)} - T_{(x_1,b/2,h-z_1)} = 0$$
$$\boldsymbol{P_2}: T_{(x_1,0,z_1)} - T_{(x_1,0,h-z_1)} = 0$$
$$\boldsymbol{P_4}: T_{(0,y_1,z_1)} + T_{(0,y_1,h-z_1)} - 2T_{O=(0,0,0)} = 0$$
$$\boldsymbol{P_8}: T_{(a/4,y_1,z_1)} + T_{(a/4,b/2-y_1,z_1)} - 2T_{(0,0,0)} = -\Delta T/2$$
$$\boldsymbol{P_6} - \boldsymbol{P_5}: T_{(x_1,y_1,0)} - T_{(x_1,y_1,h)} = 0$$

Vertices :

$$T_{1=(0,0,0)} = T_{(0,0,0)}, T_{2=(0,b/2,0)} - T_{(0,0,0)} = 0, T_{3=(0,b/2,h)} - T_{(0,0,0)} = 0,$$
$$T_{4=(0,0,h)} - T_{(0,0,0)} = 0,$$
$$T_{5=(a/4,0,0)} + T_{6=(a/4,b/2,0)} - 2T_{(0,0,0)} = -\Delta T/2,$$
$$T_{7=(a/4,b/2,h)} + T_{8=(a/4,0,h)} - 2T_{(0,0,0)} = -\Delta T/2$$

Edges parallel to z axis :

$$T_{9=(0,0,z_1)} - T_{(0,0,0)} = 0, T_{11=(0,b/2,z_1)} - T_{(0,0,0)} = 0,$$
$$T_{14=(a/4,\ b/2,\ z_1)} + T_{17=(a/4,0,z_1)} = 2T_{(0,0,0)} - \Delta T/2,$$

Edges parallel to y axis :

$$T_{10=(0,y_1,0)} - T_{(0,0,0)} = 0, T_{12=(0,y_1,h)} - T_{(0,0,0)} = 0,$$
$$T_{16=(a/4,y_1,0)} + T_{16=(a/4,b/2-y_1,0)} = 2T_{(0,0,0)} - \Delta T/2,$$
$$T_{18=(a/4,y_1,h)} + T_{18=(a/4,b/2-y_1,h)} = 2T_{(0,0,0)} - \Delta T/2$$

Edges parallel to x axis :

$$T_{13=(x_1,b/2,0)} - T_{15=(x_1,b/2,h)} = 0, T_{19=(x_1,0,0)} - T_{20=(x_1,0,h)} = 0 \quad (22)$$

Table 4
The derivation process of boundary conditions of UC_3.

Cal. cases	Boundary planes	Boundary conditions
λ_{xx}	P_1, P_2, P_4, P_5, P_6	Eq. (19) → $\boldsymbol{P_1}: T_{(x_1,b/2,z_1)} - T_{(x_1,b/2,h-z_1)} = 0$ $\boldsymbol{P_2}: T_{(x_1,0,z_1)} - T_{(x_1,0,h-z_1)} = 0$ $\boldsymbol{P_4}: T_{(0,y_1,z_1)} + T_{(0,y_1,h-z_1)} - 2T_{O=(0,0,0)} = 0$ $\boldsymbol{P_6} - \boldsymbol{P_5}: T_{(x_1,y_1,0)} - T_{(x_1,y_1,h)} = 0$
	$P_8 = (a/4, (0, b/2), z)$	$\begin{cases} \text{Eq. (5)} \rightarrow T_M - T_O = T_{O'''} - T_{M'''} \\ T_{(a/4,y_1,z_1)} - T_{O=(0,0,0)} = T_{O'''=(a/2,b/2,0)} - T_{(a/4,b/2-y_1,z_1)} \\ \text{Eq. (19)} \Rightarrow T_{O'''=(a/2,b/2,0)} = T_{6=(a/2,b/2,0)} = T_{(0,0,0)} - \Delta T/2 \end{cases}$ $\Rightarrow T_{(a/4,y_1,z_1)} + T_{(a/4,b/2-y_1,z_1)} = 2T_{(0,0,0)} - \Delta T/2$
λ_{yy}	P_1, P_2, P_4, P_5, P_6	Eq. (20) → $\boldsymbol{P_1}: T_{(x_1,b/2,z_1)} + T_{(x_1,b/2,h-z_1)} - 2T_{(0,0,0)} = -\Delta T$ $\boldsymbol{P_2}: T_{(x_1,0,z_1)} + T_{(x_1,0,h-z_1)} - 2T_{(0,0,0)} = 0$ $\boldsymbol{P_4}: T_{(0,y_1,z_1)} - T_{(0,y_1,h-z_1)} = 0$ $\boldsymbol{P_6} - \boldsymbol{P_5}: T_{(x_1,y_1,0)} - T_{(x_1,y_1,h)} = 0$
	$P_8 = (a/4, (0, b/2), z)$	$\begin{cases} \text{Eq. (5)} \rightarrow T_M - T_O = T_{O'''} - T_{M'''} \\ T_{(a/4,y_1,z_1)} - T_{O=(0,0,0)} = T_{O'''=(a/2,b/2,0)} - T_{(a/4,b/2-y_1,z_1)} \\ \text{Eq. (20)} \Rightarrow T_{O'''=(a/2,b/2,0)} = T_{6=(a/2,b/2,0)} = T_{(0,0,0)} - \Delta T/2 \end{cases}$ $\Rightarrow T_{(a/4,y_1,z_1)} + T_{(a/4,b/2-y_1,z_1)} = 2T_{(0,0,0)} - \Delta T/2$
λ_{zz}	P_1, P_2, P_4, P_5, P_6	Eq. (21) → $\boldsymbol{P_1}: T_{(x_1,b/2,z_1)} + T_{(x_1,b/2,h-z_1)} - 2T_{(0,0,0)} = -\Delta T$ $\boldsymbol{P_2}: T_{(x_1,0,z_1)} + T_{(x_1,0,h-z_1)} - 2T_{(0,0,0)} = -\Delta T$ $\boldsymbol{P_4}: T_{(0,y_1,z_1)} + T_{(0,y_1,h-z_1)} - 2T_{(0,0,0)} = -\Delta T$ $\boldsymbol{P_6} - \boldsymbol{P_5}: T_{(x_1,y_1,0)} - T_{(x_1,y_1,h)} = \Delta T$
	$P_8 = (a/4, (0, b/2), z)$	$\begin{cases} \text{Eq. (4)} \rightarrow T_M - T_O = T_{M'''} - T_{O'''} \\ T_{(a/4,y_1,z_1)} - T_{O=(0,0,0)} = T_{(a/4,b/2-y_1,z_1)} - T_{O'''=(a/2,b/2,0)} \\ \text{Eq.(21)} \Rightarrow T_{O'''=(a/2,b/2,0)} = T_{6=(a/2,\ b/2,\ 0)} = T_{(0,0,0)} \end{cases}$ $\Rightarrow T_{(a/4,y_1,z_1)} - T_{(a/4,b/2-y_1,z_1)} = 0$

For the calculation of λ_{yy}:

Boundary planes :

$\boldsymbol{P_1}: T_{(x_1,b/2,z_1)} + T_{(x_1,b/2,h-z_1)} - 2T_{(0,0,0)} = -\Delta T$

$\boldsymbol{P_2}: T_{(x_1,0,z_1)} + T_{(x_1,0,h-z_1)} - 2T_{(0,0,0)} = 0$

$\boldsymbol{P_4}: T_{(0,y_1,z_1)} - T_{(0,y_1,h-z_1)} = 0$

$\boldsymbol{P_8}: T_{(a/4,y_1,z_1)} + T_{(a/4,b/2-y_1,z_1)} - 2T_{(0,0,0)} = -\Delta T/2$

$\boldsymbol{P_6} - \boldsymbol{P_5}: T_{(x_1,y_1,0)} - T_{(x_1,y_1,h)} = 0$

Vertices :

$T_{1=(0,0,0)} = T_{(0,0,0)},\ T_{2=(0,b/2,0)} - T_{(0,0,0)} = -\Delta T/2,$

$T_{3=(0,b/2,h)} - T_{(0,0,0)} = -\Delta T/2,$

$T_{4=(0,0,h)} - T_{(0,0,0)} = 0,$

$T_{5=(a/4,0,0)} + T_{6=(a/4,b/2,0)} = 2T_{(0,0,0)} - \Delta T/2,$

$T_{7=(a/4,b/2,h)} + T_{8=(a/4,0,h)} = 2T_{(0,0,0)} - \Delta T/2$

Edges parallel to z axis :

$T_{9=(0,0,z_1)} - T_{(0,0,0)} = 0,\ T_{11=(0,b/2,z_1)} - T_{(0,0,0)} = -\Delta T/2,$

$T_{14=(a/4,b/2,z_1)} + T_{17=(a/4,0,z_1)} = 2T_{(0,0,0)} - \Delta T/2,$

Edges parallel to y axis :

$T_{10=(0,y_1,0)} - T_{12=(0,y_1,h)} = 0,$

$T_{16=(a/4,y_1,0)} + T_{16=(a/4,b/2-y_1,0)} = 2T_{(0,0,0)} - \Delta T/2,$

$T_{18=(a/4,y_1,h)} + T_{18=(a/4,b/2-y_1,h)} = 2T_{(0,0,0)} - \Delta T/2$

Edges parallel to x axis :

$T_{13=(x_1,b/2,0)} - T_{(0,0,0)} = -\Delta T/2, T_{15=(x_1,b/2,h)} - T_{(0,0,0)} = -\Delta T/2,$

$T_{19=(x_1,0,0)} - T_{(0,0,0)} = 0,\ T_{20=(x_1,0,h)} - T_{(0,0,0)} = 0$ (23)

For the calculation of λ_{zz}:

Boundary planes :

$\boldsymbol{P_1}: T_{(x_1,b/2,z_1)} + T_{(x_1,b/2,h-z_1)} - 2T_{(0,0,0)} = -\Delta T$

$\boldsymbol{P_2}: T_{(x_1,0,z_1)} + T_{(x_1,0,h-z_1)} - 2T_{(0,0,0)} = -\Delta T$

$\boldsymbol{P_4}: T_{(0,y_1,z_1)} + T_{(0,y_1,h-z_1)} - 2T_{(0,0,0)} = -\Delta T$

$\boldsymbol{P_8}: T_{(a/4,y_1,z_1)} - T_{(a/4,b/2-y_1,z_1)} = 0$

$\boldsymbol{P_6} - \boldsymbol{P_5}: T_{(x_1,y_1,0)} - T_{(x_1,y_1,h)} = \Delta T$

Vertices :

$T_{1=(0,0,0)} = T_{(0,0,0)},\ T_{2=(0,b/2,0)} - T_{(0,0,0)} = 0,$

$T_{3=(0,b/2,h)} - T_{(0,0,0)} = -\Delta T/2,$

$T_{4=(0,0,h)} - T_{(0,0,0)} = -\Delta T/2,$

$T_{5=(a/4,0,0)} - T_{6=(a/4,b/2,0)} = 0,$

$T_{7=(a/4,b/2,h)} - T_{8=(a/4,0,h)} = 0$

Edges parallel to z axis :

$T_{9=(0,0,z_1)} + T_{9=(0,0,h-z_1)} - 2T_{(0,0,0)} = -\Delta T,$

$T_{11=(0,b/2,z_1)} + T_{11=(0,b/2,h-z_1)} - 2T_{(0,0,0)} = -\Delta T,$

$T_{14=(a/4,b/2,z_1)} - T_{17=(a/4,0,z_1)} = 0$

Edges parallel to y *axis* :

$T_{10=(0,y_1,0)} - T_{(0,0,0)} = 0, T_{12=(0,y_1,h)} - T_{(0,0,0)} = -\Delta T,$

$T_{16=(a/2,y_1,0)} - T_{(0,0,0)} = 0,\ T_{18=(a/2,y_1,h)} - T_{(0,0,0)} = -\Delta T$

Edges parallel to x axis :

$T_{13=(x_1,b/2,0)} - T_{(0,0,0)} = 0,\ T_{15=(x_1,b/2,h)} - T_{(0,0,0)} = -\Delta T,$

$T_{19=(x_1,0,0)} - T_{(0,0,0)} = 0,\ T_{20=(x_1,0,h)} - T_{(0,0,0)} = -\Delta T$ (24)

In this paper, UC_1, UC_2 and UC_3 are used to establish numerical models and predict effective thermal conductivities of 3D four-directional braided composites. For the calculation of λ_{xx}, λ_{yy} and λ_{zz}, the boundary conditions of UC_1 are stated by Eqs. (1)–(3), that of UC_2 are stated by Eqs. (19)–(21), and that of UC_3 are stated by Eqs. (22)–(24), respectively. Each rotational symmetric transformation brings about its corresponding constraints and thus boundary conditions of UC_2 and UC_3 are much more complicated than that of UC_1. So it can be concluded that for rotational symmetries more utilizing of symmetric transformations means smaller size but more complicated boundary conditions of unit cells. As a matter of fact, each utilizing of rotational symmetric transformation will reduce the unit cell to a half size.

The boundary conditions indicate that for UC_2 the nodal temperature of the upper and the lower half of four lateral boundary planes, i.e., planes P_1 ($y = b/2$), P_2 ($y = 0$), P_4 ($x = 0$) and P_7 ($x = a/2$), and furthermore for UC_3 the right and the left half of

boundary plane P_8 ($x = a/4$) should be constrained by equations. In this situation, the corresponding half parts of these boundary planes should be identically meshed to apply the boundary conditions. The mesh generation will be stated in later discussion.

8. Boundary conditions of comparison calculations

The boundary conditions presented in Eqs. (1) to (3) and (19) to (24) are derived precisely according to the symmetries exhibited in the composite structure. Although these boundary conditions are accurate for certain when their rigorous derivation process is considered, they are very complicated and have to be carefully treated during the simulation. Researchers are always forced by these difficulties to search for other easier solutions. In order to confirm the necessity of accurate boundary conditions, additional calculations with the adiabatic boundary conditions are conducted in this work. The so-called adiabatic boundary condition means a temperature difference is imposed on boundary planes in the calculation direction while other four boundary planes are adiabatic, as shown in Eqs. (25) and (27) for UC_1, UC_2 and UC_3, respectively. For UC_2 and UC_3, due to the non-periodic structures of some corresponding boundary planes, e.g., P_1 and P_2 of UC_2, a constant temperature, i.e., T_1 or T_2, is imposed on these planes. This type of boundary condition is much simpler and easier to use in the simulation, however its accuracy needs to be analyzed. In the later discussion of this paper, all the results obtained by adiabatic boundary conditions are denoted by "ABC".

It should be noted that available studies focused on thermal conduction behaviours of 3D four-directional braided composites are limited, and the quarter and eighth unit cell are for the first time established in this paper. Therefore, it has to be mentioned that the main objective of these comparison calculations is to verify the significance of accurate boundary conditions rather than to indicate the possible mistakes of previous studies.

$$\begin{aligned}&\text{Calculation of } \lambda_{xx}: T_{(0,y_1,z_1)} - T_{(a,y_1,z_1)} = \Delta T\\ &\text{Calculation of } \lambda_{yy}: T_{(x_1,0,z_1)} - T_{(x_1,b,z_1)} = \Delta T\\ &\text{Calculation of } \lambda_{zz}: T_{(x_1,y_1,0)} - T_{(x_1,y_1,h)} = \Delta T\end{aligned} \tag{25}$$

$$\begin{aligned}&\text{Calculation of } \lambda_{xx}: \boldsymbol{P_4}: T_{(0,y_1,z_1)} = T_1,\ \boldsymbol{P_7}: T_{(a/2,y_1,z_1)} = T_2,\\ &\qquad\qquad T_1 - T_2 = \Delta T/2\\ &\text{Calculation of } \lambda_{yy}: \boldsymbol{P_1}: T_{(x_1,b/2,z_1)} = T_2,\ \boldsymbol{P_2}: T_{(x_1,0,z_1)} = T_1,\\ &\qquad\qquad T_1 - T_2 = \Delta T/2\\ &\text{Calculation of } \lambda_{zz}: \boldsymbol{P_6} - \boldsymbol{P_5}: T_{(x_1,y_1,0)} - T_{(x_1,y_1,h)} = \Delta T\end{aligned} \tag{26}$$

$$\begin{aligned}&\text{Calculation of } \lambda_{xx}: \boldsymbol{P_4}: T_{(0,y_1,z_1)} = T_1,\ \boldsymbol{P_8}: T_{(a/2,y_1,z_1)} = T_3,\\ &\qquad\qquad T_1 - T_3 = \Delta T/4\\ &\text{Calculation of } \lambda_{yy}: \boldsymbol{P_1}: T_{(x_1,b/2,z_1)} = T_2,\ \boldsymbol{P_2}: T_{(x_1,0,z_1)} = T_1,\\ &\qquad\qquad T_1 - T_2 = \Delta T/2\\ &\text{Calculation of } \lambda_{zz}: \boldsymbol{P_6} - \boldsymbol{P_5}: T_{(x_1,y_1,0)} - T_{(x_1,y_1,h)} = \Delta T\end{aligned} \tag{27}$$

9. Numerical models

9.1. Governing equation and model meshing

ANSYS Mechanical is used to conduct the numerical simulation. The governing equation is:

$$\lambda_{xx}\frac{\partial^2 T}{\partial x^2} + \lambda_{yy}\frac{\partial^2 T}{\partial y^2} + \lambda_{zz}\frac{\partial^2 T}{\partial z^2} + (\lambda_{xy} + \lambda_{yx})\frac{\partial^2 T}{\partial x \partial y} + (\lambda_{xz} + \lambda_{zx})\frac{\partial^2 T}{\partial x \partial z} + (\lambda_{yz} + \lambda_{zy})\frac{\partial^2 T}{\partial y \partial z} = 0 \tag{28}$$

where λ_{xx} etc. are the non-isotropic thermal conductivities.

Based on Eq. (28), the temperature distributions can be calculated, and thus the effective thermal conductivities of the composite can be obtained by Eq. (29):

$$\begin{aligned}q_x^o &= -\lambda_{xx}^o T_x^o - \lambda_{xy}^o T_y^o - \lambda_{xz}^o T_z^o\\ q_y^o &= -\lambda_{yx}^o T_x^o - \lambda_{yy}^o T_y^o - \lambda_{yz}^o T_z^o\\ q_z^o &= -\lambda_{zx}^o T_x^o - \lambda_{zy}^o T_y^o - \lambda_{zz}^o T_z^o\end{aligned} \tag{29}$$

T_x^o, T_y^o and T_z^o are temperature gradients in three component directions applied as boundary conditions, and the matrix element λ_{xx}^o, λ_{xy}^o, λ_{xz}^o ... are effective thermal conductivities to be calculated in which non-diagonal elements λ_{xy}^o, λ_{xz}^o ... equal to 0 according to the authors' previous work [16]. q_x^o, q_y^o and q_z^o are the heat flux in

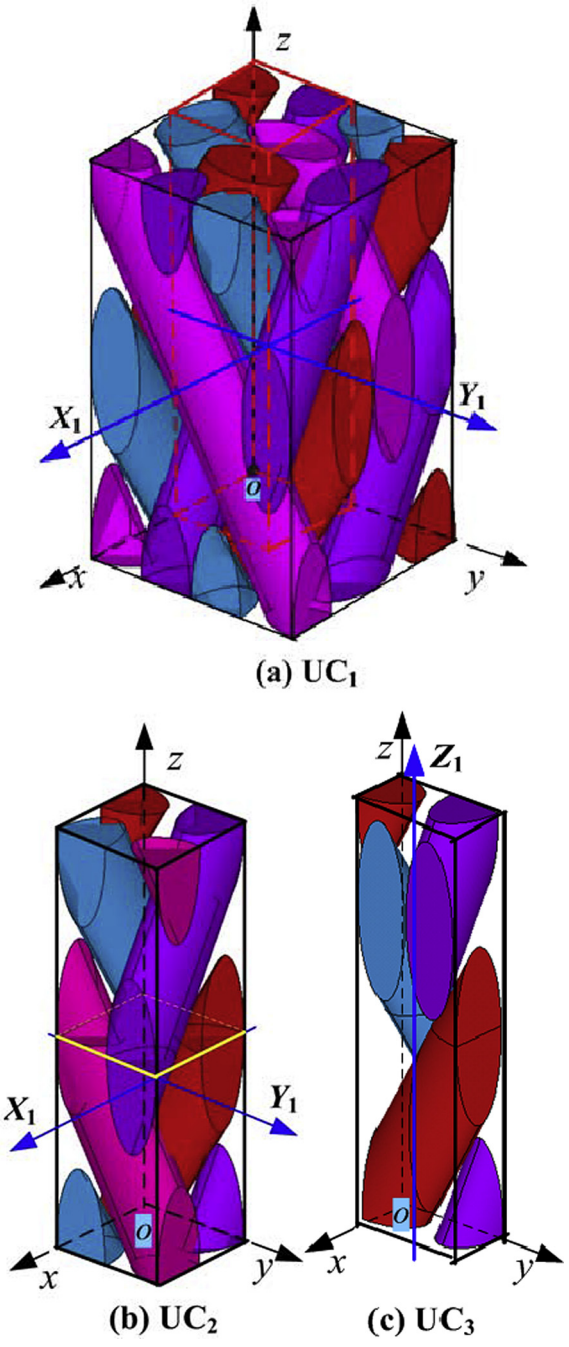

Fig. 7. Numerical models of 3D four-directional braided composites.

three component directions and can be obtained by Q_i/A_i, where Q_i is the heat flow through the corresponding boundary plane and A_i is the area of the plane.

Figs. 1–4 are the topological models and the establishment of numerical models needs additional information about the yarns' shape and size as detailed stated in [16]. In this paper, the cross-section of braiding yarns is assumed to be ellipse, models established based on UC_1, UC_2 and UC_3 can be seen in Figs. 7 (a), (b) and (c), respectively, in which the fiber volume fraction, V_f is 0.5 and the interior braiding angle, γ is 35°. In order to exhibit the distribution of braiding yarns clearly the matrix is not shown in the figures.

For UC_1, the boundary conditions require the same grid for corresponding planes, i.e., the plane groups: $x = 0$ and $x = a$, $y = 0$ and $y = b$, $z = 0$ and $z = h$. For UC_2, the plane groups should be: $(0, y, (h/2, h))$ and $(0, y, (0, h/2))$, $(a/2, y, (h/2, h))$ and $(a/2, y, (0, h/2))$, $(x, 0, (h/2, h))$ and $(x, 0, (0, h/2))$, $(x, b/2, (h/2, h))$ and $(x, b/2, (0, h/2))$, $z = 0$ and $z = h$. For UC_3, the plane groups should be: $(0, y, (h/2, h))$ and $(0, y, (0, h/2))$, $(a/4, (0, b/4), z)$ and $(a/4, (b/4, b/2), z)$, $(x, 0, (h/2, h))$ and $(x, 0, (0, h/2))$, $(x, b/2, (h/2, h))$ and $(x, b/2, (0, h/2))$, $z = 0$ and $z = h$. We use APDL (ANSYS Parametric Design Language) command MSHCOPY to realize the copy and paste of the area mesh of corresponding planes. Based on the area mesh, the volumes are meshed with 3D thermal solid element SOLID 70 and the meshed models are shown in Fig. 8(a)–(c). Also, as shown in Fig. 8 (b) and (c), the mesh of small area depicted by yellow dash lines is displayed in the enlarged picture and the identical mesh is indicated more distinctly. Although different number of grids will be generated for models with different V_f and γ, in this work UC_1 has about 3,000,000 elements and 500,000 nodes, UC_2 has about 700,000 elements and 130,000 nodes, while UC_3 has about 400,000 elements and 80,000 nodes. The obtained numerical result is independent of mesh refinement in this work.

Table 5
Materials properties.

	Transverse thermal conductivity/(W/(m·K))	Axial thermal conductivity/(W/(m·K))
Carbon fiber	0.675	7.81
Resin	0.178	0.178

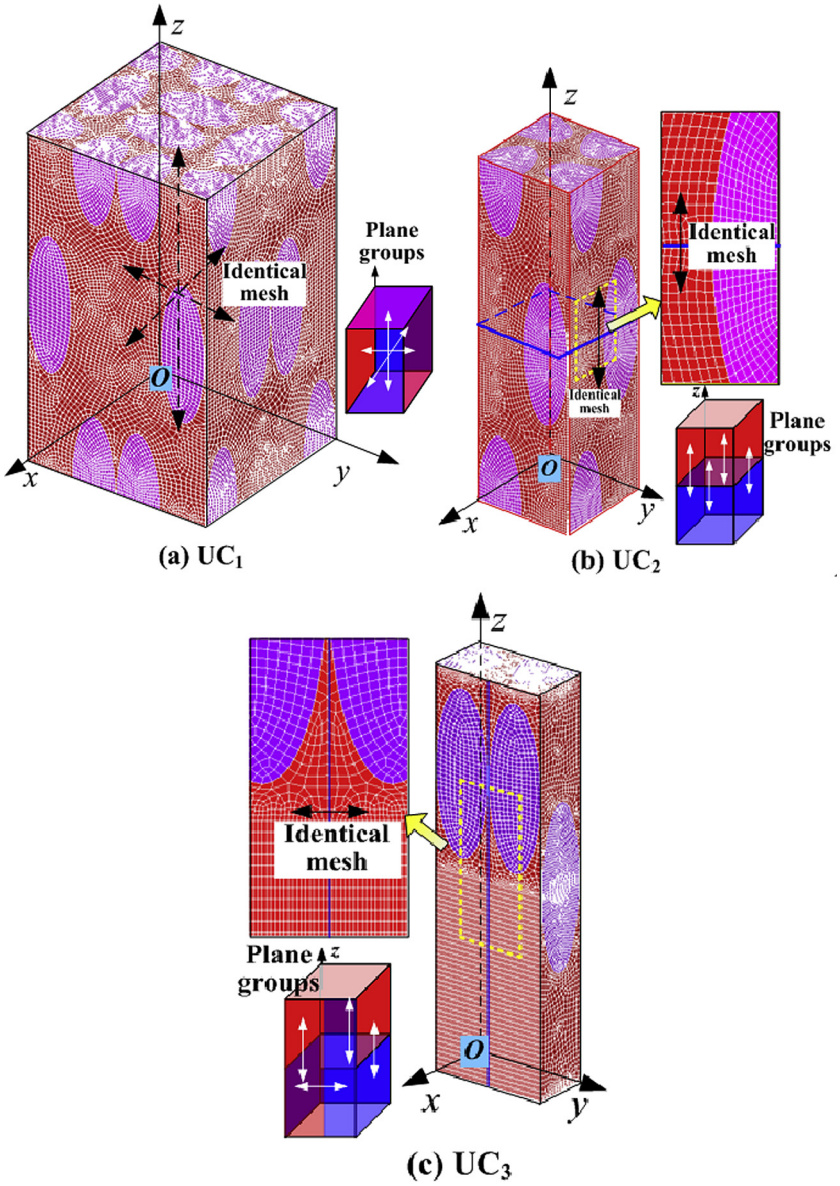

Fig. 8. Meshed models.

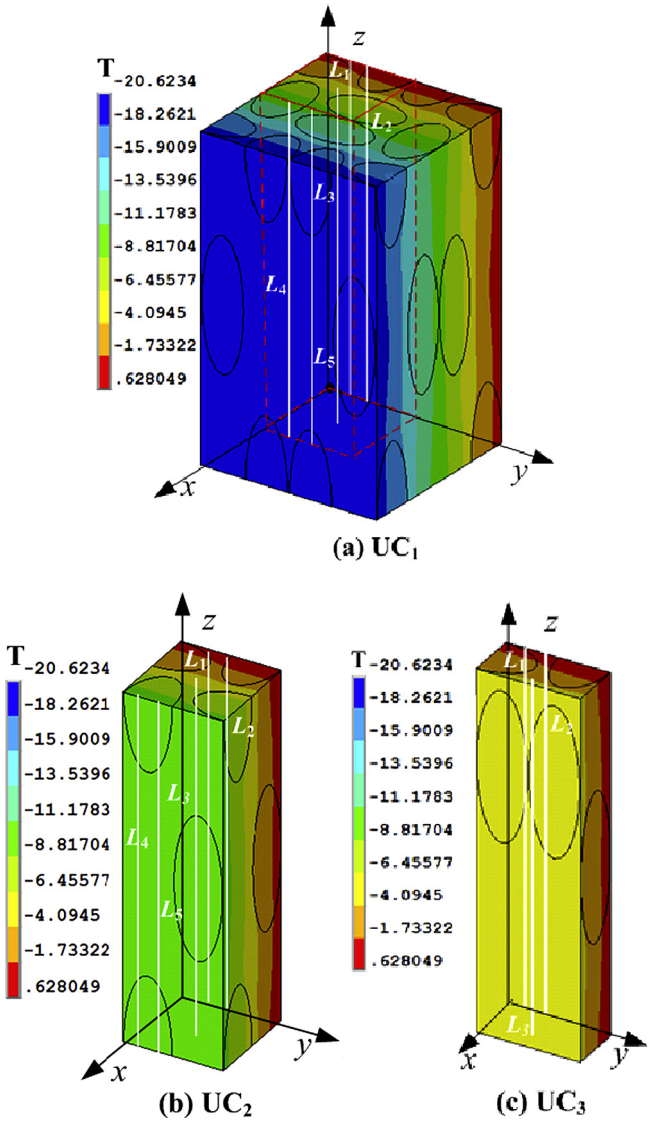

Fig. 9. Temperature fields of volumes for the calculation of λ^o_{xx}.

9.2. Materials properties

In this work, the matrix of the composite is epoxy resin TDE-86 and the reinforcing fiber is T300 carbon. The thermal properties can be seen in Table 5. The braiding yarn consists of resin and carbon fibers, and its axial and transverse thermal conductivities can be calculated by:

$$\lambda_{ya} = \lambda_{fa} V_{fy} + \lambda_m (1 - V_{fy}) \tag{30}$$

$$\lambda_{yt} = \lambda_m + \frac{V_{fy}}{1/(\lambda_{ft} - \lambda_m) + (1 - V_{fy})/(2\lambda_m)} \tag{31}$$

where λ_{ya} and λ_{yt} are the axial and transverse thermal conductivity of yarns, respectively. λ_{fa} and λ_{ft} are the axial and transverse thermal conductivity of fibers, respectively. λ_m is the thermal conductivity of resin. V_{fy} is the fiber volume fraction of yarns, and can be calculated by V_f/V_y where V_y is the yarn volume fraction of composites. Eq. (31) is referred to in [28] and its accuracy is validated by FEM simulations in [16].

It should be noted that the temperature is a very important factor affecting the composite effective thermal conductivity. However, only normal temperature environment is considered in this work, since the accurate prediction of effective thermal conductivities needs accurate essential input data, i.e., thermal conductivities of the resin and the carbon, which are very difficult to obtain at low or high temperatures. On the other hand, according to the above discussion we can see that the model and the boundary conditions will not be affected by the environment temperature. Considering it from a positive point of view this work proposed an approach which can be used to predict effective properties of composites at any temperatures provided that the accurate input data can be obtained.

10. Results and discussions

10.1. Temperature fields

10.1.1. Accurate boundary conditions

Temperature distributions of volumes, planes and lines are displayed to illustrate the same numerical results obtained by three different unit cells. Figs. 9 (a), (b) and (c) are temperature fields of volumes obtained by three unit cells for the calculation of λ^o_{xx}

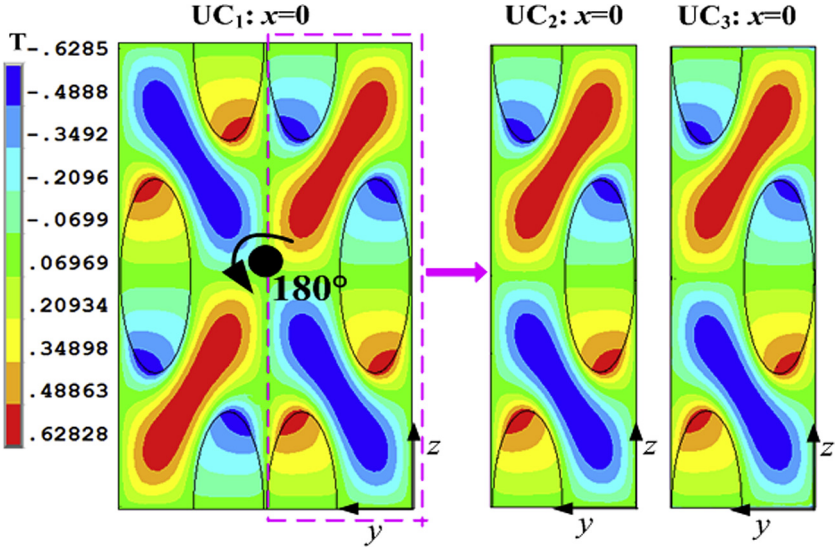

Fig. 10. Temperature fields at boundary planes $x = 0$ for the calculation of λ^o_{xx}.

($V_f = 0.5$, $\gamma = 30°$). From boundary conditions of UC_2 and UC_3 one can notice that T_O acts as a reference temperature. Therefore, in order to compare temperature fields obtained by the different unit cells, T_O is set to 0 °C for the specific cases ($V_f = 0.5$, $\gamma = 30°$). As shown in the figures, under the same legend all the temperature fields are relatively uniform and have very similar distributions. Fig. 10 shows the temperature fields at boundary planes $x = 0$ by three unit cells with the same legend (UC_2 and UC_3 have the same size of plane $x = 0$). The black point indicates rotation axis X_1-axis, and the temperature field of UC_1 displays an obvious distribution of 180° rotation symmetry between the left and the right parts. Also, the almost identical temperature distributions are obtained by three unit cells. In order to further confirm that UC_1, UC_2 and UC_3 result in the certainly same temperature fields, the temperatures of nodes on path lines $L_1 = (0, b/8, z)$, $L_2 = (0, b/4, z)$, $L_3 = (a/4, b/4, z)$, $L_4 = (a/2, b/8, z)$ and $L_5 = (a/2, b/4, z)$ (the white lines in Fig. 9) are extracted and shown in Fig. 11. It should be noted that UC_3 only has path lines L_1, L_2 and L_3. The solid, the dash and the dash dot lines represent results obtained by UC_1, UC_2 and UC_3, respectively, and different colours indicate different path lines. The solid, the dash and the dash dot lines almost coincide with each other and the largest difference which has an absolute value of 0.035 °C while a relative one of only 0.7%, occurs on the path line L_3 and is between UC_2 and UC_3. Although the difference is very small, there is something interesting and it deserves an analysis and discussion. For UC_3, L_3 is on the boundary plane P_8 (see Fig. 6) and its temperature distribution is described by the boundary conditions shown in Eq. (22). Considering Eq. (22) carefully one can find that all the nodal temperatures on L_3 are accurately constrained as -5 °C. However, for UC_1 and UC_2, L_3 is in the interior region and its temperature distribution is obtained during the numerical calculation. The calculated temperature on L_3 fluctuates around -5 (the accurate value) with a largest deviation of 0.7%. At this condition, the difference of the temperature fields obtained by three unit cells might be due to the numerical error rather than the reduced size of unit cells or their complicated boundary conditions.

One can also find a uniform volume temperature field for the calculation of λ^o_{zz} as shown in Fig. 12. Temperature distributions at boundary planes of z direction (planes $z = h$) are shown in Fig. 13. In the figure, the pink point represents axis $Z_1 = (a/4, b/4, z)$, and 180° rotational symmetries about Z_1 of temperature distribution can be observed in the results of UC_1 and UC_2. In addition, the temperature fields obtained by three different unit cells are very similar to each other under the same legend.

From Figs. 9–13 it can be concluded that three different unit cells result in the same temperature fields and this indicates the reliability of the boundary conditions derived for UC_2 and UC_3 in this work.

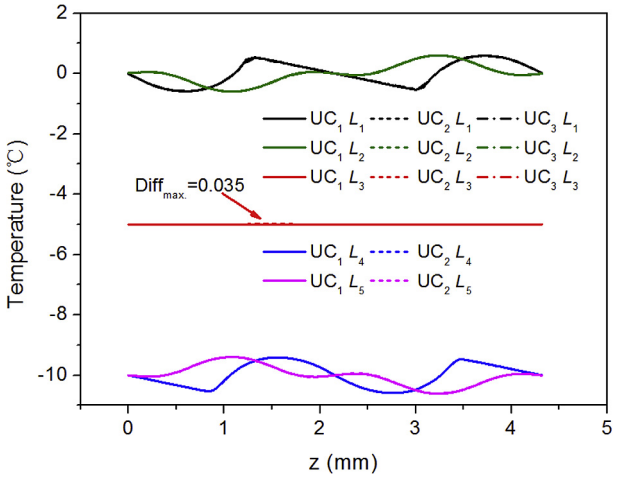

Fig. 11. Temperature on path lines for the calculation of λ^o_{xx}.

10.1.2. Comparison with inappropriate boundary conditions

In fact, we can conclude that the temperature distribution calculated by models with boundary conditions presented in this paper can completely represent the full structure of composite, especially when we consider the rigorous derivation process of boundary conditions. On the other hand, these types of boundary conditions are relatively tedious and complicated to use in the simulation, and thus its necessity has to be clarified here. Some calculations with inappropriate boundary conditions described in Eqs. (25) to (27) are conducted to state the deviation between results obtained by different boundary conditions.

Fig. 14 is the temperature fields for the calculation of λ^o_{zz} obtained by adiabatic boundary conditions. In the figure, "ABC" means the adiabatic boundary conditions for UC_1, UC_2 and UC_3 as shown in Eqs. (25)–(27), respectively. Compared with the uniform distribution obtained by accurate boundary conditions (see

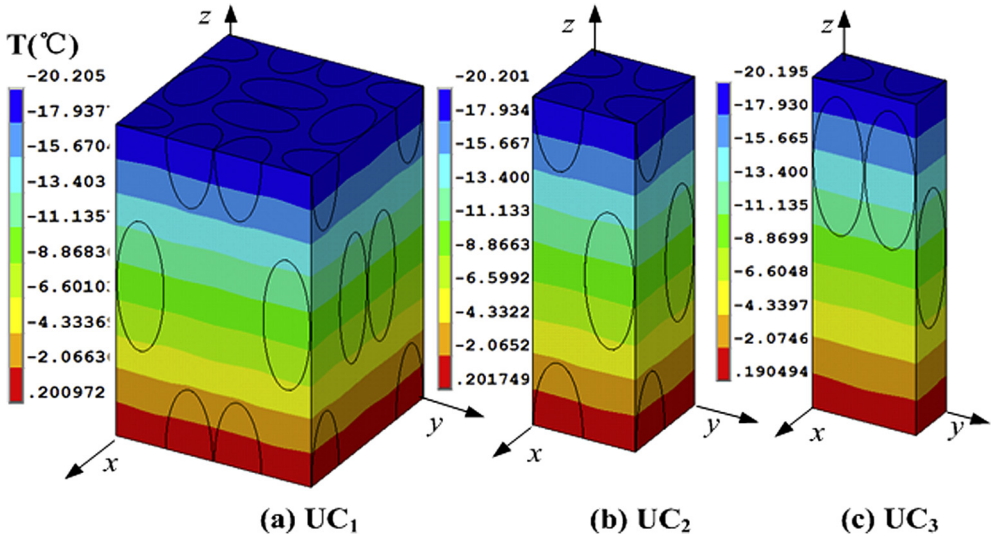

Fig. 12. Temperature fields of volumes for the calculation of λ^o_{zz}.

Fig. 12), the temperature fields obtained by adiabatic boundary conditions have a much different distribution, and also three unit cells lead to totally different results. The temperature on path lines also has the same condition, take UC_2 as an example, Fig. 15 shows the temperature of nodes on lines L_1 to L_5 obtained by UC_2 with different boundary conditions. In the figure, "DBC" means the boundary conditions derived in this paper. The nodal temperatures on the five lines by "DBC" unit cell have the same and a nearly linear distribution, while those by "ABC" unit cell have different nonlinear distributions. From Figs. 12–15 one can find that the inappropriate adiabatic boundary conditions will lead to a wrong temperature distribution much different from the real condition and may influence its accuracy of the prediction of effective thermal conductivity and will be discussed later.

10.2. Effective thermal conductivities

Based on the three models, effective thermal conductivities of 3D four-directional braided composites are numerically calculated. The fiber volume fraction V_f is assumed to be 0.4, 0.5 and 0.58, and the interior braiding angle γ varies from 15° to 50°. Figs. 16 and 17 are the transverse ($\lambda^o_{xx} = \lambda^o_{yy}$) and the axial ($\lambda^o_{zz}$) thermal conductivities obtained by three models. The black solid lines with black solid symbols, the red dash line with red solid symbols, and the green dot line with green solid symbols are the results obtained by UC_1, UC_2 and UC_3 with derived boundary conditions,

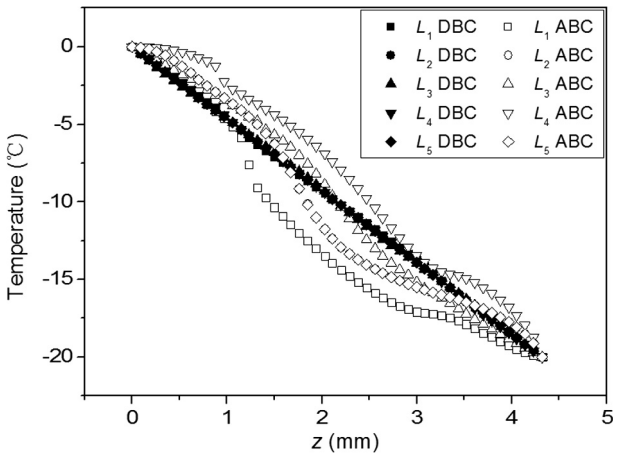

Fig. 15. Temperature on path lines of UC_2 with different boundary conditions.

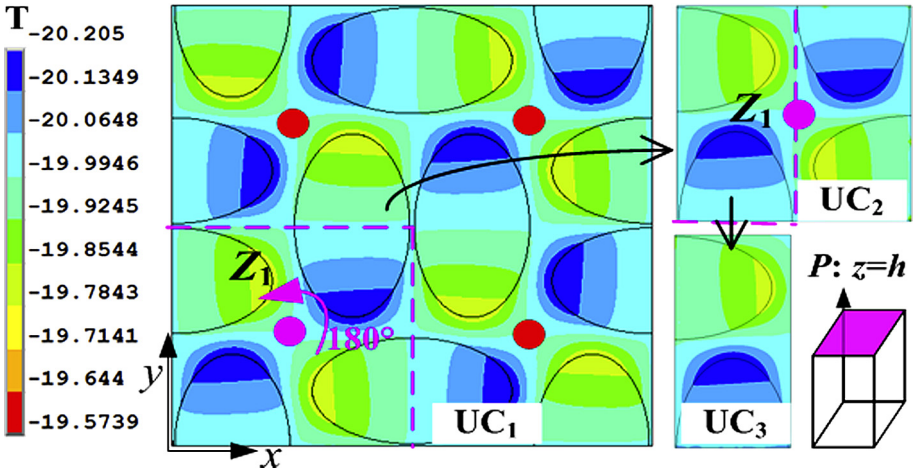

Fig. 13. Temperature fields at boundary planes $z = h$ for the calculation of λ^o_{zz}.

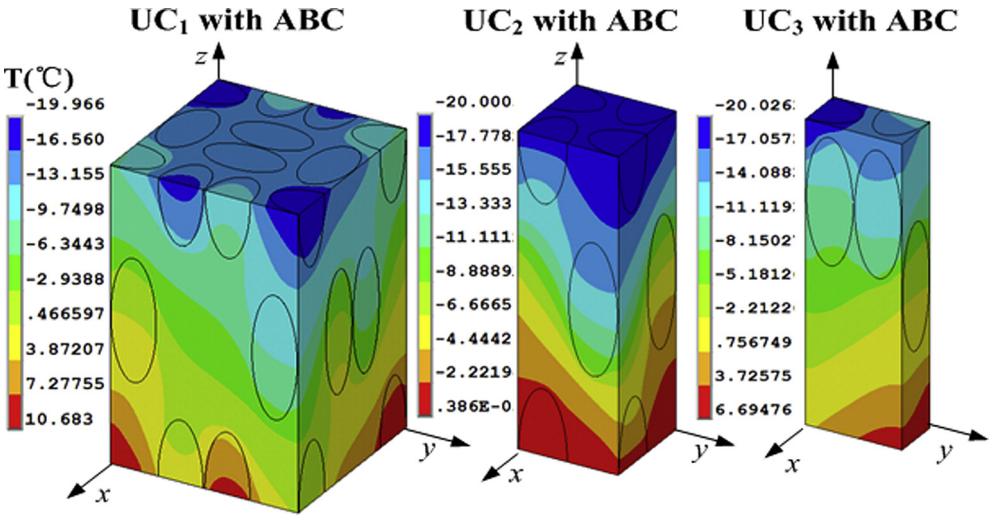

Fig. 14. Temperature fields obtained by adiabatic boundary conditions.

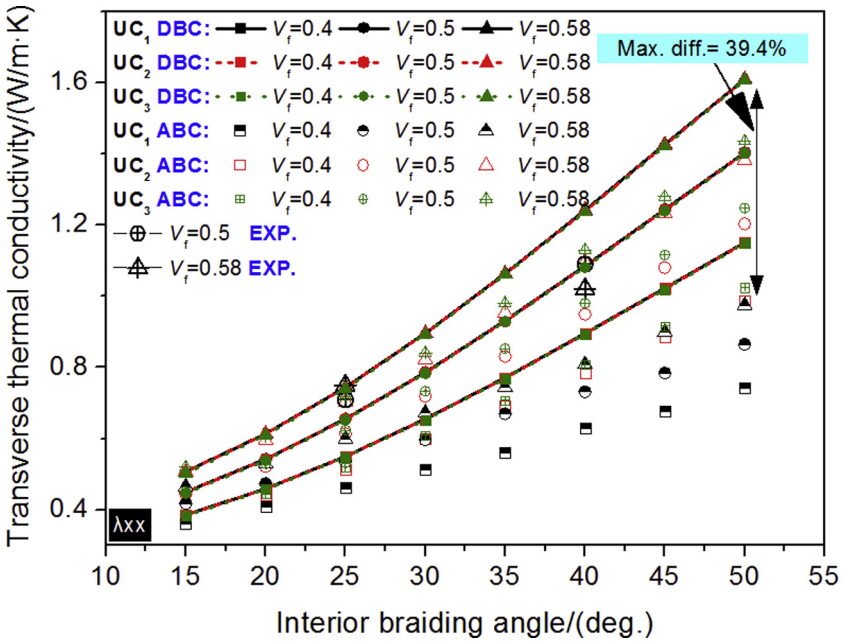

Fig. 16. Transverse thermal conductivities of composites.

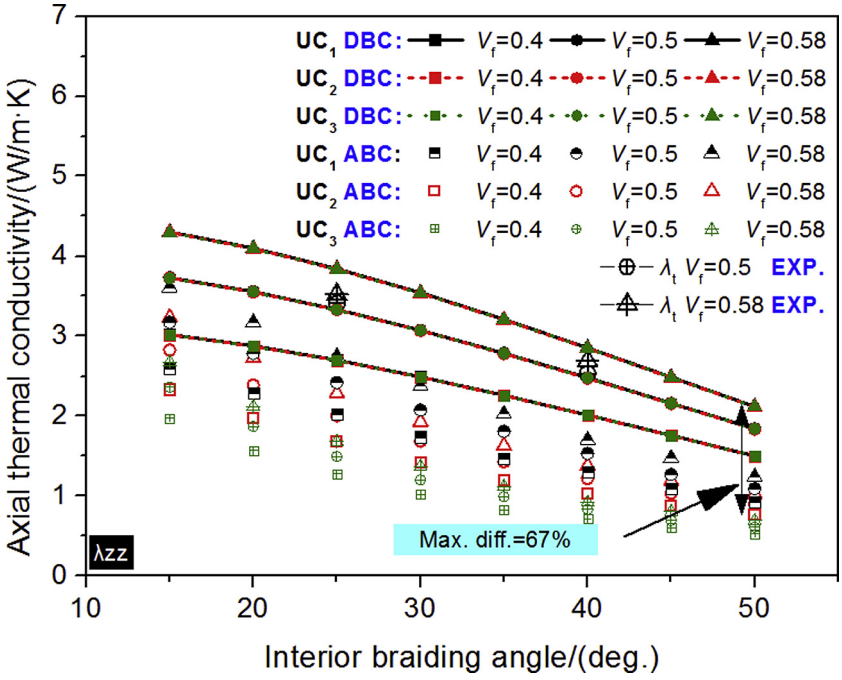

Fig. 17. Axial thermal conductivities of composites.

respectively. The symbols without lines are results calculated by adiabatic boundary conditions. From the figures one can see that with the increase of fiber volume fraction both the effective transverse and axial thermal conductivities of composites increase, since the fiber has larger thermal conductivities than the matrix resin. As for the interior braiding angle, the angle between the fiber yarns and the axial direction, a larger value means that the transverse projection of fiber yarns is longer while the axial component is shorter, and thus the increasing interior braiding angle leads to the increase of transverse but the decrease of axial thermal conductivities. Additionally, effective thermal conductivities obtained by three models with accurate boundary conditions approach each other greatly with a maximum difference of 0.3% (λ_{zz}^{o} for $V_f = 0.5$, $\gamma = 50°$). This further validates the accuracy of boundary conditions derived for UC_2 and UC_3 in this paper. Furthermore, the computational time required for UC_2 and UC_3 is only about 25% and 12.5% of UC_1 (about an hour for a Dell work station with 8 CPUs and 24 GB RAM). So, compared with UC_1, UC_2 and UC_3 have much more complicated boundary conditions while at the same time a smaller size and a great saving of computational cost.

On the other hand, as discussed above the temperature distribution obtained by adiabatic boundary conditions has much difference with that of the derived boundary conditions. From Figs. 16 and 17 one can see that also the effective thermal conductivities

Table 6
Comparison with experimental results.

V_f	γ	λ_{xx} (UC_1)	λ_{xx} (UC_2)	λ_{xx} (UC_3)	λ_t (Exp.)	Diff. (Max.) (%)	λ_{zz} (UC_1)	λ_{zz} (UC_2)	λ_{zz} (UC_3)	λ_a (Exp.)	Diff. (Max.) (%)
0.5	25	0.656	0.655	0.653	0.709	−7.62	3.334	3.328	3.33	3.41	−2.4
0.5	40	1.085	1.084	1.082	1.09	−0.55	2.480	2.475	2.477	2.53	−2.17
0.58	25	0.744	0.744	0.741	0.75	−0.8	3.843	3.837	3.839	3.52	9.18
0.58	40	1.241	1.239	1.236	1.021	21.6	2.854	2.847	2.851	2.692	6.02

Table 7
Comparison with experimental results (numerical results with ABC).

V_f	γ	λ_t (Exp.)	λ_{xx} (UC_1)	Diff. (%)	λ^o_{xx} (UC_2)	Diff. (%)	λ^o_{xx} (UC_3)	Diff. (%)
0.5	25	0.709	0.536	−24.4	0.614	−13.4	0.624	−12.0
0.5	40	1.09	0.732	−32.8	0.949	−12.9	0.98	−10.1
0.58	25	0.75	0.599	−20.1	0.704	−6.13	0.717	−4.4
0.58	40	1.021	0.809	−20.8	1.097	7.44	1.13	10.7
V_f	γ	λ_a (Exp.)	λ^o_{zz} (UC_1)	Diff. (%)	λ^o_{zz} (UC_2)	Diff. (%)	λ^o_{zz} (UC_3)	Diff. (%)
0.5	25	3.41	2.421	−29.0	2.007	−41.1	1.494	−56.2
0.5	40	2.53	1.534	−39.4	1.221	−51.7	0.835	−67.0
0.58	25	3.52	2.745	−22.0	2.287	−35.0	1.681	−52.2
0.58	40	2.692	1.703	−36.7	1.378	−48.8	0.9231	−65.7

obtained by adiabatic boundary conditions (the "ABC" symbols without lines in Figs. 16 and 17) have much deviation with that of derived boundary conditions. For transverse thermal conductivities, the maximum deviation is about 39.4%, while for axial thermal conductivities the maximum deviation is about 67%. This indicates that the accurate boundary condition is very important for the prediction of composites' effective thermal conductivities by unit cells.

The predicted thermal conductivities are compared with results measured by a hot disk analyser (TPS2500S) presented in the authors' previous work [16]. Four types of composites with different interior braiding angle and fiber volume fraction as listed in Table 6 are measured. During the braiding process, the length and width of braided pitch, which can represent the size of the meso structure of composite, are controlled to obtain the composite materials with the same interior braiding angle but different fiber volume fraction. As shown in Table 6, except the transverse thermal conductivity of the last sample ($V_f = 0.58$, $\gamma = 40°$), the numerical and experimental values have relatively good agreement with a maximum difference of 9.18%. This comparison validates the reliability of the numerical models established in this work. For the larger deviation of transverse thermal conductivity of the last sample, the measured value is smaller than the second sample which has a smaller fiber volume fraction and means an unreasonable value. This may be due to the material's manufactering defect. Also, the results calculated by inappropriate boundary conditions (adiabatic BC) are compared with the experimental results as shown in Table 7. The calculation error in Table 7 is much larger than that in Table 6 and the maximum one reaches an unacceptable value of −39.4% for UC_1, −51.7% for UC_2 and −67% for UC_3, respectively.

As discussed above, for unit cells established in this paper, the derived appropriate boundary conditions result in accurate effective thermal conductivities, while the inappropriate boundary conditions lead to un-neglected errors. The boundary conditions are closely related with the validity of the unit cell. In fact, the effective properties of composites can only be calculated based on a model which contains enough and complete information (structure, constituents, etc.) about the composite. We can establish a relative infinite model of the same structure and size with the experimental specimen, or a micro representative volume element (unit cells) of the specimen. For the relative infinite model, the adiabatic boundary condition similar to Eq. (25) which is often imposed during the real steady-state experimental measurement can be used in the calculation, and the accurate results will be obtained for sure. However, the establishment of such a model is difficult and even impossible for its great computational cost. On the other hand, once a unit cell as presented in this work is established, the additional boundary conditions have to be derived to enable the unit cell be an adequately representative to the composite, and for most cases the adiabatic boundary conditions will not be appropriate any longer.

11. Conclusions

It is for the first time a quarter and an eighth unit cell of three-dimensional four-directional braided composite are formulated by using three 180° rotational transformations. The thermal boundary conditions of each unit cell corresponding to each transformation are precisely derived. Based on the full, the quarter and the eighth unit cell the effective thermal conductivities of the composites are predicted. The identical temperature distributions and effective thermal conductivities (difference less than 0.3%) obtained by the three unit cells verify the accuracy of the boundary conditions. The good agreement between numerical and experimental results indicates the reliability of the numerical models. The numerical results show some conclusions:

(1) Each rotational symmetric transformation can formulate a unit cell in half size and a reducing-size unit cell has more complicated thermal boundary conditions, however at the same time can bring about a great saving of the computational source. The computational time required for the quarter and the eighth unit cell in this work is about only 25% and 12.5% of the full unit cell.
(2) In the prediction of thermal conduction behaviours for three-dimensional four-directional braided composites, accurate boundary conditions have to be derived rigorously according to the symmetric transformations. Inappropriate boundary conditions will lead to a wrong prediction of temperature distribution and an inappropriate evaluation of effective thermal conductivities with a possible unacceptable error.

Acknowledgment

This study is supported by the Key Project of International Joint Research of National Natural Science Foundation of China (51320105004) and 111 Project (B16038).

References

[1] Mouritz AP, Bannister MK, Falzon PJ, Leong KH. Review of applications for advanced three-dimensional fibre textile composites. Compos A Appl Sci Manuf 1999;30(12):1445–61.
[2] Zhou H, Zhang W, Liu T, Gu B, Sun B. Finite element analyses on transverse impact behaviors of 3-D circular braided composite tubes with different braiding angles. Compos A Appl Sci Manuf 2015;79:52–62.
[3] Zhang M, Sun B, Gu B. Accelerated thermal ageing of epoxy resin and 3-D carbon fiber/epoxy braided composites. Compos A Appl Sci Manuf 2016;85:163–71.
[4] Dong K, Zhang J, Jin L, Gu B, Sun B. Multi-scale finite element analyses on the thermal conductive behaviors of 3D braided composites. Compos Struct 2016;143:9–22.
[5] Chen L, Tao XM, Choy CL. On the microstructure of three-dimensional braided preforms. Compos Sci Technol 1999;59(3):391–404.
[6] Wu DL. Three-cell model and 5D braided structural composites. Compos Sci Technol 1996;56(3):225–33.
[7] He XL, Wang R, Liu C, Zhang QQ. Ultrasonic nondestructive testing analysis of 3D 5-directional braided composites. Adv Mater Res 2013;601:50–3.
[8] Zeng T, Wu LZ, Guo LC. Mechanical analysis of 3D braided composites: a finite element model. Compos Struct 2004;64(3–4):399–404.
[9] Sun XK, Sun CJ. Mechanical properties of three-dimensional braided composites. Compos Struct 2004;65(3–4):485–92.
[10] Fang GD, Liang J, Wang Y, Wang BL. The effect of yarn distortion on the mechanical properties of 3D four-directional braided composites. Compos A Appl Sci Manuf 2009;40(4):343–50.
[11] Zhang C, Xu XW. Finite element analysis of 3D braided composites based on three unit-cells models. Compos Struct 2013;98:130–42.
[12] Zeng T, Wu LZ, Guo LC. A finite element model for failure analysis of 3D braided composites. Mater Sci Eng A Struct Mater Prop Microstruct Process 2004;366(1):144–51.
[13] Fang GD, Liang J, Wang BL. Progressive damage and nonlinear analysis of 3D four-directional braided composites under unidirectional tension. Compos Struct 2009;89(1):126–33.
[14] Lu ZX, Wang CY, Xia B, Zhou Y. Effect of interfacial properties on the thermophysical properties of 3D braided composites: 3D multiscale finite element study. Polym Compos 2013;35(9):1690–700.
[15] Jiang LL, Xu GD, Cheng S, Lu XM, Zeng T. Predicting the thermal conductivity and temperature distribution in 3D braided composites. Compos Struct 2014;108:578–83.
[16] Gou JJ, Zhang H, Dai YJ, Li S, Tao WQ. Numerical prediction of effective thermal conductivities of 3D four-directional braided composites. Compos Struct 2015;125:499–508.
[17] Fang WZ, Chen L, Gou JJ, Tao WQ. Predictions of effective thermal conductivities for three-dimensional four-directional braided composites using the lattice Boltzmann method. Int J Heat Mass Transf 2016;92:120–30.
[18] Li S, Wongsto A. Unit cells for micromechanical analyses of particle-reinforced composites. Mech Mater 2004;36(7):543–72.
[19] Li S. General unit cells for micromechanical analyses of unidirectional composites. Compos Part A Appl Sci Manuf 2001;32(6):815–26.
[20] Wongsto A, Li S. Micromechanical FE analysis of UD fibre-reinforced composites with fibres distributed at random over the transverse cross-section. Compos A Appl Sci Manuf 2005;36(9):1246–66.
[21] Whitcomb JD, Chapman CD, Tang XD. Derivation of boundary conditions for micromechanics analyses of plain and satin weave composites. J Compos Mater 2000;34(9):724–47.
[22] Tang XD, Whitcomb JD. General techniques for exploiting periodicity and symmetries in micromechanics analysis of textile composites. J Compos Mater 2003;37(13):1167–89.
[23] Li S, Zhou C, Yu H, Li L. Formulation of a unit cell of a reduced size for plain weave textile composites. Comput Mater Sci 2011;50(5):1770–80.
[24] Li S, Warrior N, Zou Z, Almaskari F. A unit cell for FE analysis of materials with the microstructure of a staggered pattern. Compos A Appl Sci Manuf 2011;42(7):801–11.
[25] Gou JJ, Dai YJ, Li S, Tao WQ. Numerical study of effective thermal conductivities of plain woven composites by unit cells of different sizes. Int J Heat Mass Transf 2015;91:829–40.
[26] Li DS, Fang DN, Jiang N, Yao XF. Finite element modeling of mechanical properties of 3D five-directional rectangular braided composites. Compos B Eng 2011;42(6):1373–85.
[27] Li DS, Lu ZX, Chen L, Li JL. Microstructure and mechanical properties of three-dimensional five-directional braided composites. Int J Solids Struct 2009;46(18–19):3422–32.
[28] Hashin Z. Analysis of composite materials-a survey. J Appl Mech Trans ASME 1983;50(3):481–505.